

**The Kinetics of Austenite Formation during  
Continuous Heating of a Multi-Phase Steel**

by

YEONG-BONG CHO

B. Eng., Pusan National University, Korea, 1990

A THESIS SUBMITTED IN PARTIAL FULFILLMENT OF THE  
REQUIREMENTS FOR THE DEGREE OF

MASTER OF APPLIED SCIENCE

in

THE FACULTY OF GRADUATE STUDIES

(Department of Metals and Materials Engineering)

We accept this thesis as conforming  
to the required standard

THE UNIVERSITY OF BRITISH COLUMBIA

May, 2000

© Yeong-Bong Cho, 2000

In presenting this thesis in partial fulfilment of the requirements for an advanced degree at the University of British Columbia, I agree that the Library shall make it freely available for reference and study. I further agree that permission for extensive copying of this thesis for scholarly purposes may be granted by the head of my department or by his or her representatives. It is understood that copying or publication of this thesis for financial gain shall not be allowed without my written permission.

Department of Metals & Materials Eng.  
The University of British Columbia  
Vancouver, Canada

Date May 19<sup>th</sup>, 2000

## **ABSTRACT**

DP (Dual-Phase) and TRIP (Transformation Induced Plasticity) steels, also known as multi-phase steels, have been attracting a growing interest in the development of lighter automobiles owing to their excellent combination of strength and ductility. TRIP steels can usually be generated from a standard cold-rolled ferrite-pearlite grade by a two stage continuous annealing process; continuous heating and intercritical annealing, followed by subsequent cooling and austempering. The material is first intercritically annealed in the ferrite/ austenite coexistence region, during which the ferrite matrix recrystallizes and austenite is created. Austempering is then performed and some upper bainite is formed, which, in turn, stabilizes the remaining austenite even down to room temperature.

Most studies have been focused so far on the second stage of the thermal scheme due to the fact that the steel properties depend primarily on the transformation processes following austenitization. However, the phase transformations occurring upon heating is of profound importance. The state of the microstructure after heating; i.e., volume fraction, shape, distribution and chemical composition of the austenite grains, has a great influence on the kinetics of the phase transformation during cooling and on the subsequent mechanical properties of the steel. Furthermore, the kinetics of the reverse transformation to austenite

determine the time and temperature required for either intercritical heat treatment or normalization.

The objective of the present study is to characterize and understand the reaustenitization kinetics from pearlite-ferrite structure during continuous heating. Further, a mathematical model based on the Avrami equation and the additivity principle has been adopted in modeling the pearlite-ferrite to austenite transformation during continuous heating.

# TABLE OF CONTENTS

ABSTRACT .....	ii
LIST OF FIGURES .....	vi
LIST OF TABLES .....	ix
LIST OF SYMBOLS.....	x
ACKNOWLEDGEMENTS.....	xv
<b>CHAPTER 1 – INTRODUCTION.....</b>	<b>1</b>
<b>CHAPTER 2 – LITERATURE REVIEW .....</b>	<b>6</b>
2.1 DP and TRIP Steel .....	6
2.1.1 General Characteristics .....	6
2.1.2 TRIP Phenomenon .....	7
2.1.3 Influence of Alloying Elements .....	11
2.1.4 Processing and Microstructure.....	15
2.2 Microstructural Aspects of Austenitization.....	18
2.3 Modeling of Austenitization .....	22
2.3.1 Avrami Equation .....	22
2.3.2 The Principle of Additivity.....	23
2.3.3 Diffusion Model .....	31
<b>CHAPTER 3 – EXPERIMENTAL WORK .....</b>	<b>35</b>
3.1 Materials.....	35
3.2 Experimental Techniques .....	36
3.2.1 Continuous Heating Tests .....	36
3.2.2 Microstructural Investigation.....	42
3.2.3 Microhardness Measurements .....	44

<b>CHAPTER 4 – RESULTS AND DISCUSSION</b> .....	45
4.1 Initial Microstructures.....	45
4.2 CHT Data Analysis.....	47
4.3 Effect of Heating Rate .....	56
4.4 Effect of Initial Microstructure.....	61
4.5 Microstructural Change During Heating.....	63
4.6 Effect of Recrystallization .....	68
<b>CHAPTER 5 - KINETICS MODELING</b> .....	74
5.1 Prediction of $A_1$ and $A_3$ Temperatures.....	74
5.2 Modeling of Continuous Heating Kinetics.....	75
5.2.1 Application of the Additivity Rule .....	75
5.2.2 Comparison of Model and Experimental Data.....	81
<b>CHAPTER 6 – CONCLUSIONS AND FUTURE WORK</b> .....	88
6.1 Conclusions.....	88
6.2 Comments on Future Work .....	90
<b>REFERENCES</b> .....	91

## LIST OF FIGURES

Figure 1-1 : Strength-Elongation balance for different HSLA steels [3] .....	2
Figure 2-1 : Typical stress-strain curves for high-strength automotive strip [19].....	6
Figure 2-2 : Schematic illustration showing chemical free energy of austenite and martensite as a function of temperature [60].....	9
Figure 2-3 : Schematic illustration showing the critical stress for martensite formation as a function of temperature [60] .....	9
Figure 2-4 : Fe-Fe <sub>3</sub> C phase diagram [44].....	13
Figure 2-5 : Schematic drawing of the intercritical annealing process for producing DP and TRIP steels and carbon enrichment [2].....	17
Figure 2-6 : SEM micrograph of the typical microstructure of the industrially produced TRIP steel [41].....	17
Figure 2-7 : Potential austenite nucleation sites in a pearlitic microstructure: interlamellar (site A), colony boundary (site B), and colony edge (site C) [77] .....	19
Figure 2-8 : Schematic illustration of the use of the additivity principle for the prediction of continuous heating kinetics, showing a series of isothermal transformation curves and their relationship to a stepped transformation event [77] .....	29
Figure 2-9 : Diagram showing the approximation of continuous heating kinetics as the sum of a series of short duration isothermal increments [77].....	30
Figure 2-10 : Representation of the one-dimensional domain [0, L] (spherical geometry), of the solute profiles in the $\alpha$ and $\gamma$ regions and the corresponding equilibrium phase diagram [44] .....	34
Figure 3-1 : The specimen chamber and basic components of the Gleeble 1500 Thermomechanical simulator [98] .....	39

Figure 3-2 : The specimen design for the Gleeble used in the CHT experiments .....	39
Figure 3-3 : Experimental dilation versus temperature results for a continuous heating test conducted at 1°C/s for the HR specimen. The solid lines indicate the extrapolations from the pre- and post-transformation regions .....	40
Figure 4-1 : Optical micrographs of starting microstructures (nital etch).....	46
Figure 4-2 : The austenite fraction vs. temperature curves showing a typical variation of transformation kinetics [HR material, 30°C/s].....	49
Figure 4-3 : Example of data analysis [HR material, 30°C/s]; (a) criteria for data selection, (b) dilation vs. temperature curves.....	52
Figure 4-4 : Examples of the curve fitting for the HR material in which the total transformation curves are divided into two separate curves, i.e., P→ $\gamma$ and $\alpha$ → $\gamma$ .....	54
Figure 4-5 : The averaged transformation curve for 30°C/s heating rate of the HR material .....	55
Figure 4-6 : Effect of heating rate on continuous heating kinetics.....	57
Figure 4-7 : $T_S$ and $T_F$ temperatures as a function of heating rates for different initial structures .....	58
Figure 4-8 : Transformation start and finish times as a function of heating rates for the HR material.....	60
Figure 4-9 : Effect of initial microstructures on continuous heating kinetics with selected heating rates .....	62
Figure 4-10(a): Microstructural changes during continuous heating with a 1°C/s heating rate for various helium quenching temperatures (QT); (a) HR material.....	65
Figure 4-10(b): Microstructural changes during continuous heating with a 1°C/s heating rate for various helium quenching temperatures (QT); (b) 50CR material.....	66

Figure 4-11 : Comparison of dilation test results and metallographic examinations for the austenite volume fraction transformed for (a) HR material and (b) 50CR material .....	67
Figure 4-12(a): Microstructures helium quenched from 745°C for various heating rates (hr); (a) HR material.....	70
Figure 4-12(b): Microstructures helium quenched from 745°C for various heating rates (hr); (b) 50CR material .....	71
Figure 4-13 : Microhardness changes of ferrite for various heating rates for the CR materials which were helium quenched from 745°C .....	72
Figure 4-14 : Comparison of CHT kinetics between the HR and recrystallized 50CR materials for different heating rates.....	73
Figure 5-1 : Fitted $\ln b$ values as a function of temperatures for (a) $P \rightarrow \gamma$ and (b) $\alpha \rightarrow \gamma$ transformation of the HR material .....	78
Figure 5-2 : Schematic diagram showing the calculation procedure to predict continuous heating kinetics for the $P \rightarrow \gamma$ transformation by assuming additive isothermal conditions.....	82
Figure 5-3 : Comparison between experimental data and predicted continuous heating kinetics for the HR material .....	85
Figure 5-4 : Comparison between experimental data and predicted continuous heating kinetics for the 20CR material .....	86
Figure 5-5 : Comparison between experimental data and predicted continuous heating kinetics for the 50CR material .....	87

## LIST OF TABLES

Table 2.1 : Values of $n$ in the Avrami equation [90] .....	23
Table 3.1 : Chemical compositions (in wt. %) of the steel investigated .....	36
Table 3.2 : Experimental conditions of continuous heating tests.....	36
Table 4.1 : Dilation data of the HR material with a 30°C/s heating rate .....	51
Table 5.1 : $A_1$ and $A_3$ temperatures (°C) calculated for 0.16C-1.38Mn-0.24Si steel using methods developed by Andrews [45] and Kirkaldy and Baganis [54] .....	75
Table 5.2 : Calculated kinetic parameters for modeling the continuous heating transformations of the HR, 20CR, and 50CR materials.....	80

## LIST OF SYMBOLS

$a$	half-thickness of the pearlite slab
$A_{c1}$	ferrite to austenite transformation start temperature during heating (= $T_{Ac1}$ )
$A_{c3}$	ferrite to austenite transformation finish temperature during heating (= $T_{Ac3}$ )
$A_{e1}$	equilibrium temperature between austenite and pearlite (= $T_{Ae1}$ )
$A_{e3}$	equilibrium temperature between austenite and ferrite (= $T_{Ae3}$ )
$X'_{F,N1}$	normalized volume fraction of ferrite transformed at $T_1$ but heated and now present at $T_2$
$\alpha$	ferrite
$\alpha'$	martensite
$\alpha_\alpha$	thermal expansion coefficient of ferrite
$\alpha_\gamma$	thermal expansion coefficient of austenite
$\alpha/\gamma$	interface between ferrite and austenite
$\alpha_{mix}$	mixed thermal expansion coefficient during the $\alpha \rightarrow \gamma$ transformation
$\alpha \rightarrow \gamma$	ferrite to austenite transformation
$b$	Avrami equation rate constant
$b_F$	Avrami equation rate constant for $\alpha \rightarrow \gamma$ transformation

$b_P$	Avrami equation rate constant for P $\rightarrow$ $\gamma$ transformation
$B_s$	bainite transformation start temperature
$C_\alpha^*$	carbon concentration at the interface in the $\alpha$ domain
$C_\gamma^*$	carbon concentration at the interface in the $\gamma$ domain
$C_v$	carbon concentration in the phase $v$
$d$	diameter of the ferrite grain
$D_\alpha$	ferrite diametric response extrapolated into two phase region
$\Delta G_{M_s}^{\gamma \rightarrow \alpha'}$	free energy difference between $\gamma$ and $\alpha'$ at the $M_s$ temperature
$\Delta t$	time interval
$\Delta V$	volume change
$D_\gamma$	austenite diametric response extrapolated into two phase region
$D_0$	initial diametric response at room temperature
$D(T)$	diametric response at temperature T
$D_v$	carbon diffusion coefficient in the phase $v$
$F_i$	ferrite volume fraction of the initial structure
$G$	growth rate
$\gamma$	austenite
$G(X)$	general function of fraction transformed
$H(T)$	general function of temperature
HV	Vickers hardness

$M_d$	a temperature above which the martensite transformation does not occur regardless of the applied amount of stress and strain
$M_s$	martensite transformation start temperature
$M_s^\sigma$	the highest temperature at which martensite transformation occurs elastically with an increase of applied stresses
$n$	Avrami equation time exponent
$n_F$	Avrami equation time exponent for $\alpha \rightarrow \gamma$ transformation
$n_P$	Avrami equation time exponent for $P \rightarrow \gamma$ transformation
$P_i$	pearlite volume fraction of the initial structure
$P+\alpha \rightarrow \gamma$	pearlite-ferrite to austenite transformation
$P/\gamma$	interface between pearlite and austenite
$P$	pearlite
$P \rightarrow \gamma$	pearlite to austenite transformation
$t_2'$	time to produce volume fraction $X_{F,N1}$ , at $T_2$
$T_{\alpha 0}$	selected temperature in the ferrite region for analysis of dilation data
$t_a(T)$	isothermal time to reach a specific fraction transformed
$t_{AV_{CHT.F}}$	start time for $\alpha \rightarrow \gamma$ transformation under continuous heating conditions
$T$	temperature
$T_0$	equilibrium temperature between austenite and ferrite
$T_F$	transformation finish temperature

$T_{\gamma 0}$	selected temperature in the austenite region for analysis of dilation data
$t$	time
$T_S$	transformation start temperature
$t_v$	virtual time which is the time to reach the current fraction transformed
$U'$	mechanical driving force for the $\gamma \rightarrow \alpha'$ transformation
$V$	volume
$V_0$	initial volume at room temperature
$V_v(P)$	volume fraction of pearlite
$X$	fraction transformed
$X_A$	true volume fraction of austenite calculated by the Avrami equation and additivity principle
$X_{A,NI}$	normalized volume fraction of austenite formed at temperature $T_1$
$X_{A,T1}$	true volume fraction of austenite formed at temperature $T_1$
$X_{eq}$	equilibrium volume fraction
$X_F$	ferrite volume fraction transformed
$X_{F,NI}$	normalized volume fraction of ferrite transformed at temperature $T_1$
$X_{P,NI}$	normalized volume fraction of pearlite transformed at temperature $T_1$
$X_P$	pearlite volume fraction transformed
$X_{P,T1}$	true volume fraction of pearlite transformed at temperature $T_1$

*This thesis is dedicated*

*to*

*the memory of my father*

## **ACKNOWLEDGMENTS**

I would like to express my sincere thanks to my supervisor Dr. Matthias Militzer for his utmost support and guidance throughout the course of this research. Special thanks to Mr. B. Chau, Mr. R. Cardeno, and Ms. J. Kitchen for their assistance.

I acknowledge with thanks the financial support provided by POSCO, Pohang Iron and Steel Co., Ltd. Further thanks to all the members of the cold rolling department in Pohang works who supported and helped me during my study. Especially, I would like to convey many thanks to Mr. Dong-Seob Lee, Mr. Seon-Hwan Ahn, Mr. Young-Jing Sohn, Mr. Kwang-Jae Yoo, Mr. Soon-Tae Jeong, Mr. Jeong-Min Park, Mr. Byeong-Ryul Jeon, and Mr. Jee-Su Chang for their generous support and encouragement in helping me achieve my academic and professional goals through this work. I am also grateful to Dr. Sang-Rae Lee, Dr. Seung-Bin Kim, Dr. Sung-Ho Park, Mr. Young-Ho Cho, Mr. Dae-In Jung, Dr. Joon-Hyeong Jang, Dr. Tae-Yeob Kim, Mr. Hyun-Tae Kim, and Mr. Jae-Ryung Lee for their various kinds of assistance.

Finally I would like to thank all my family and friends, especially my mother, my parents-in-law, my wife, my daughter and son, for their great sacrifices and patience through my study. They have been a source of wisdom, understanding and strength throughout my research.

## **CHAPTER 1 – INTRODUCTION**

In the last decades, many types of high-strength high-formable steels have been developed for automotive application in response to the conflicting demands for safety and weight reduction. These steels must possess higher strengths without loss of formability in order to expand the range of application to more critical parts. In the past, the strength of steels for automotive industry was increased mainly by thermomechanical processing leading to a combination of solid-solution hardening, grain refinement, and precipitation hardening. The resulting steels have been successfully adopted to diverse applications in automotive construction [1]. However, it is generally found that increasing the strength of these steels results in a penalty regarding their cold formability, as can be seen in Figure 1-1. This means that the higher strength steels cannot be used in complicated pressformed parts. A further problem is the increasing deformation resistance during rolling, so that the required low thickness cannot be produced. This has led to the development of multi-phase steels which have an excellent combination of strength and ductility as shown in Figure 1-1.

In these steels, the material properties are adjusted by a tailored combination of different microstructure components such as ferrite, austenite, bainite, and martensite. One example are the well-known DP (Dual-Phase) steels [2] where, for example, approximately 5 to 20% of hard martensite is enclosed in the basic ferrite matrix. With minimum tensile strength of

500 - 600 MPa and 20 - 30% elongation, dual-phase steels cover the lower tensile strength range of the multi-phase steels.

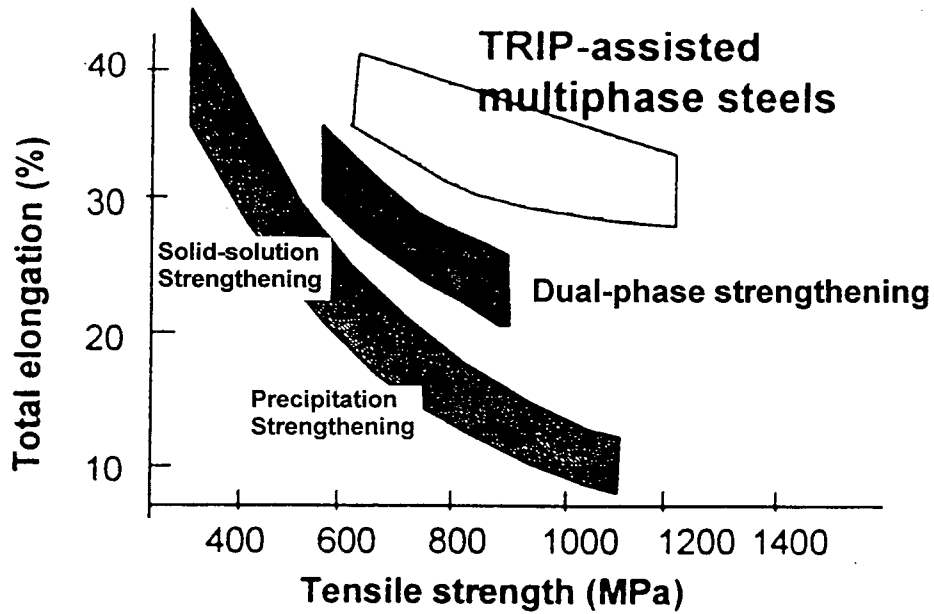


**Figure 1-1: Strength-Elongation balance for different HSLA steels [3]**

A further development are the so-called TRIP (Transformation Induced Plasticity) steels [3] which have tensile strengths in the range of 600 - 1000 MPa and 30 - 40% elongation. The microstructure of the TRIP steels usually consists of a fine dispersion of metastable retained austenite in the basic ferrite/bainite matrix, which are transformed to hard martensite during subsequent forming.

Such a sophisticated multiphase structure can usually be generated from a standard cold-rolled ferrite-pearlitic grade by a two stage heat treatment process; continuous heating and intercritical annealing, followed by subsequent cooling and austempering. The material is first intercritically annealed in the ferrite/austenite coexistence domain, during which the ferrite matrix recrystallizes and austenite is created. Subsequently, austempering is applied and some upper bainite is formed, which, in turn, stabilizes the remaining austenite even down to room temperature.

Reaustenitization, i.e., the reverse transformation to austenite upon heating, is an inevitable occurrence during the heat treatment of steels. The microstructure which is developed during intercritical heat treatment for multi-phase steels is strongly dependent upon the kinetics of this transformation. Despite this consideration, less attention has been paid so far to the study of the formation of austenite as compared with the vast amount of research on its decomposition process during the second stage of the thermal scheme. It is possible to make a guess at why this situation has arisen. First, the austenite formed during reaustenitization is usually destroyed by subsequent transformation during cooling to ambient temperatures, and therefore direct observation of the austenite formed is almost impossible. Second, experimental studies of the kinetics of reaustenitization are hampered by a dependency on the composition, size and distribution of the parent phases. This means that the starting microstructure must be carefully characterized prior to heat treatment.

However, the phase transformations occurring upon heating is of profound importance. The state of the microstructure after heating; i.e., volume fraction, shape, distribution and chemical composition of the austenite grains, has a great influence on the kinetics of the phase transformation during cooling and on the subsequent mechanical properties of the steel. Furthermore, the kinetics of the reverse transformation to austenite determine the time and temperature required for either intercritical heat treatment or normalization.

Although the formation of austenite in low alloy steels has been the subject of several investigations [4-13], there has been little systematic work done on the reaustenitization process in low carbon multi-phase steels and these studies are generally restricted to describe single phase transformations such as pearlite-to-austenite, ferrite-to-austenite or bainite-to-austenite. In this sense, the present work was undertaken to study the transformation behavior of multi-phase steels during continuous heating. The main point of interest in this study is the microstructural evolution during continuous heating, in particular the kinetics of the formation of austenite. The transformation kinetics were characterized by microstructural observation and dilatometric analysis which is a generally accepted technique to study phase transformations in steels. Several different initial microstructures were incorporated into this study; these included as-received hot rolled, 20% and 50% cold rolled as well as a fully bainitic structure.

Computer modeling has increasingly become a useful tool in predicting microstructural changes and final mechanical properties. Umemoto [14], for example, devised a nucleation and growth model for austenite-to-ferrite transformation for a continuous cooling process. Suehiro et al.[15] and Saito [16] built integrated models for microstructure prediction. This type of computational analysis based on thermodynamics can provide a powerful tool to understand a complicated transformation behavior such as that in multi-phase steels, when effectively combined with conventional metallurgical analysis. Here, a mathematical model based on the Avrami equation and the additivity principle has been adopted in modeling the pearlite-ferrite to austenite transformation during continuous heating.

The present study was undertaken to characterize the reaustenitization kinetics in a plain carbon multi-phase steel. There are two major objectives:

1. to examine the effect of heating rates and starting microstructures on the austenite fraction transformed by continuous heating tests.
2. to develop a mathematical model to describe the kinetics of austenite formation from a pearlite-ferrite initial structure.

## CHAPTER 2 – LITERATURE REVIEW

### 2.1 DP and TRIP Steel

#### 2.1.1 General Characteristics

DP (Dual Phase) and TRIP (Transformation Induced Plasticity) steels, also known as multi-phase steels, are considered promising materials for the automotive and steel industries because of their excellent strength and formability relationships [17, 19]. These steels are characterized by a high tensile strength, low yield strength, high initial work hardening rate, no yield point elongation, and high total elongation, as illustrated in Figure 2-1.

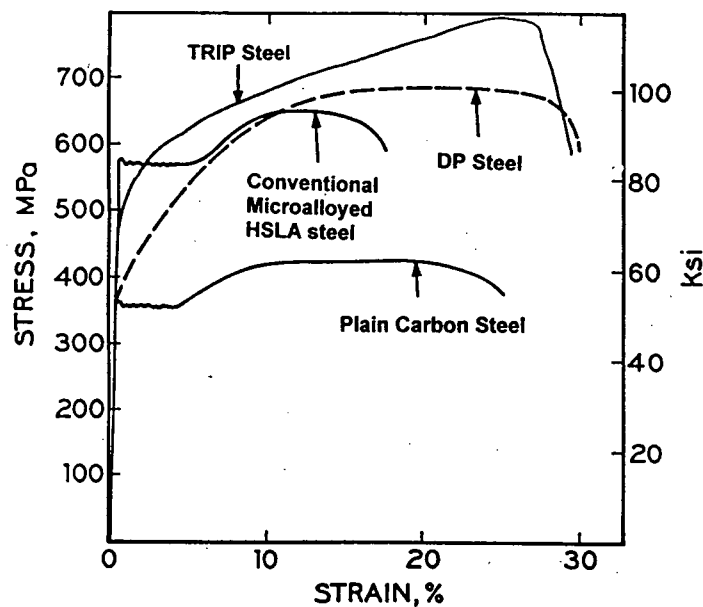


Figure 2-1 : Typical stress-strain curves for high-strength automotive strip [19]

### 2.1.2 TRIP Phenomenon

The TRIP effect was discovered by Zackay et al. in 1967 [57] in Ni-Cr steels containing 7.6 - 8.3% Ni and 8.8 - 9.0% Cr. The excellent combination of strength and ductility of TRIP steels is based on the stress-assisted and strain-induced martensitic transformation of retained austenite during deformation [36, 40, 58, 59].

Figure 2-2 [60] shows schematically the change in chemical free energies of martensite and austenite with temperature.  $T_o$  is the temperature at which the austenite and martensite are in equilibrium, and  $M_s$  is the highest temperature at which martensite forms spontaneously upon cooling. Austenite (the parent phase) will not decompose into martensite unless the free energy of austenite is larger than the free energy of martensite. This excess in free energy of the austenite over that of the martensite may be regarded as the 'driving force' behind the martensite transformation. The austenite ( $\gamma$ ) to martensite ( $\alpha'$ ) transformation does not start just below  $T_o$ , but at a substantially lower temperature where enough free energy is available from the transformation to account for the strain energy that is an inevitable product of the reaction [61].

The difference in free energies between austenite and martensite,  $\Delta G_{M_s}^{\gamma \rightarrow \alpha'}$  at the  $M_s$  temperature, is the critical chemical driving force for the onset of the martensitic transformation. In Figure 2-2, if an external stress is applied to the austenite at  $T_l$  (between

$M_s$  and  $T_0$ ), the mechanical driving force ( $U'$ ) due to the stress is added to the chemical driving force ( $\Delta G_{T_1}^{\gamma \rightarrow \alpha'}$ ) and the martensitic transformation starts at the critical stress where the total driving force is equal to  $\Delta G_{M_s}^{\gamma \rightarrow \alpha'}$ .  $U'$  in Figure 2-2 ( $=\Delta G_{M_s}^{\gamma \rightarrow \alpha'} - \Delta G_{T_1}^{\gamma \rightarrow \alpha'}$ ) is the critical mechanical driving force necessary for the stress-induced martensitic transformation at  $T_1$ . On the other hand, the martensitic transformation does not occur above a certain temperature,  $M_d$ , regardless of the amount of stress and strain, i.e., the martensitic transformation only occurs between  $M_s$  and  $M_d$  temperature. The transformation caused by an external stress is called "deformation induced transformation".

Concerning the role of plastic deformation of austenite on the deformation-induced martensitic transformation, there have been two different views; stress-assisted and strain-induced martensite transformation, as shown schematically in Figure 2-3 [60].

Applied stresses are significant because of the role of dislocations in both nucleation and growth mechanisms. The chemical driving force ( $\Delta G^{\gamma \rightarrow \alpha'}$ ) decreases linearly with an increase in temperature above  $M_s$ , as shown in Figure 2-2. Thus, it can be expected that the critical applied stress for the start of martensite formation increases linearly with temperature in the range between  $M_s$  and  $M_s^\sigma$ , as shown in Figure 2-3.  $M_s^\sigma$  is the highest temperature at which martensite transformation occurs elastically with an increase of applied stresses.

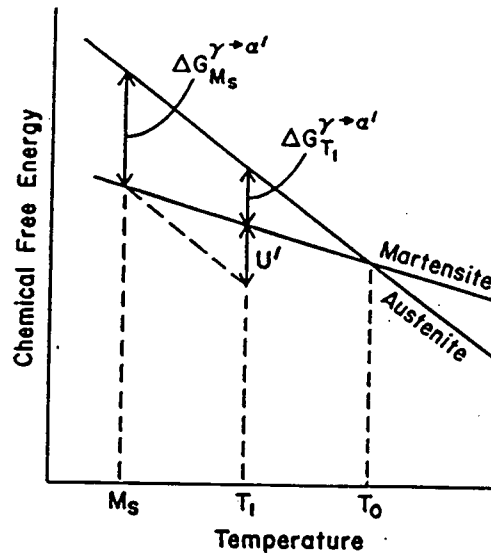


Figure 2-2 : Schematic illustration showing chemical free energies of austenite and martensite as a function of temperature [60]

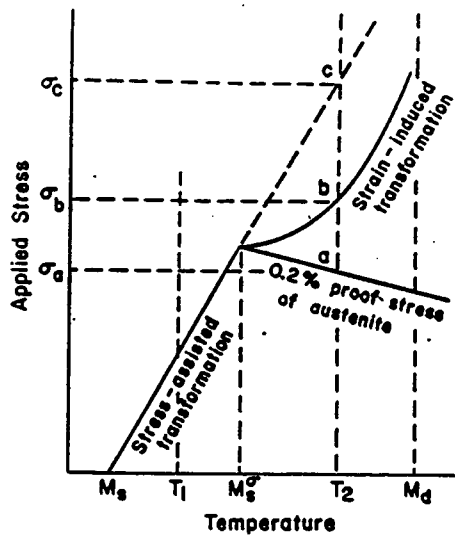


Figure 2-3 : Schematic illustration showing the critical stress for martensite formation as a function of temperature [60]

However, during deformation above  $M_s^\sigma$  (e.g., at  $T_2$  in Figure 2-3), stress concentration occurs at obstacles (e.g., grain boundaries, twin boundaries, etc.) and this applied stress provides stress-assisted transformation, i.e., when the macroscopic applied stress is  $\sigma_b$ , the largest stress locally concentrated at obstacles is equivalent to  $\sigma_c$  [62].

The other hypothesis is the strain-induced martensite transformation. Above  $M_s^\sigma$  temperature, for instance at  $T_2$  in Figure 2-3, the austenite begins to deform plastically at a stress  $\sigma_a$  and is strain-hardened until  $\sigma_b$ ; then the martensitic transformation starts to take place. That is, transformation is preceded by yielding in the austenite and both strain-induced transformation and slip become modes of plasticity [63].  $\sigma_b$  is considerably lower than  $\sigma_c$ , which is expected by extrapolating the critical stress-temperature line between  $M_s$  and  $M_s^\sigma$ . This decrease (i.e.,  $\sigma_c - \sigma_b$ ) of critical applied stress for martensitic formation is due to plastic deformation of austenite in which new nucleation sites are created through plastic strain and operate by the applied stress. Hence, nucleation at lower driving forces, i.e., nucleation with the applied stress less than  $\sigma_c$  in Figure 2-3, is possible during strain-induced transformation.

According to Maxwell et al. [64], the TRIP effect is ascribed to strain-induced martensite, not to the stress-assisted one. The high toughness comes from a combination of high strength and ductility which is a direct consequence of the strain-induced martensite transformation. If a certain region is severely deformed plastically, strain-induced

transformation takes place, increasing the local work-hardening rate and inhibiting an incipient neck from further growth. Therefore, a remarkable increase in elongation is obtained between  $M_s^\sigma$  and  $M_d$ , the temperature range where the martensite is formed during deformation, which is called transformation-induced plasticity.

### ***2.1.3 Influence of Alloying Elements***

The major alloying elements for the DP and TRIP steels are carbon, manganese, and silicon. The chemistry of DP steels falls in the range of 0.04- 0.2 wt% C, 1- 1.5 wt% Mn and 0.2- 0.4 wt% Si [20-35]. The chemical composition of TRIP steels is usually in the range of 0.1- 0.2 wt.% C, 1-2 wt% Mn, and 1-2 wt% Si [36-40]. In order for TRIP to occur at room temperature,  $M_s^\sigma$  of the steel should be just below room temperature [60]. Therefore, for TRIP steels used at room temperature, large amount of Mn, Si, Ni, and Cr are necessary in order to stabilize the austenite and lower  $M_s^\sigma$  to about room temperature. However, there is a trend to replace Si by Al, P etc. because silicon is known to cause surface defects after casting and to form adherent hard oxides not compatible with the industrial surface cleaning practice prior to hot rolling. Furthermore, steel compositions require low silicon contents in order to allow galvanization and spot welding [41].

The alloying elements have influence on both the thermodynamics and kinetics of the phase transformation occurring in those steels. The addition of the alloying elements Mn and Si to a plain carbon steel produces several important changes [42, 43]. First, their presence alters the phase boundaries in the Fe-Fe<sub>3</sub>C phase diagram (Figure 2-4).

Empirical formulae have been developed to describe the effect of alloying elements on the  $A_{e3}$ ,  $A_{c1}$ , and  $A_{c3}$  temperatures [45],

$$A_{e3} = 910 - 25Mn - 11Cr - 20Cu + 60Si + 60Mo + 40W + 100V + 700P + 3 \\ - (250Al + 120As + 400Ti) + f(C, Ni) \quad (2.1)$$

where the “3” represents the effect of sulfur, which was assumed to give a constant rise in the Ae3 temperature, and  $f(C, Ni)$  is a tabulated function of the  $C$  and  $Ni$  levels.

$$A_{c1} = 723 - 10.7Mn - 16.9Ni + 29.1Si + 16.9Cr + 290As + 6.38W \quad (2.2)$$

$$A_{c3} = 910 - 203\sqrt{C} - 15.2Ni + 44.7Si + 104V + 31.5Mo + 13.1W \quad (2.3)$$

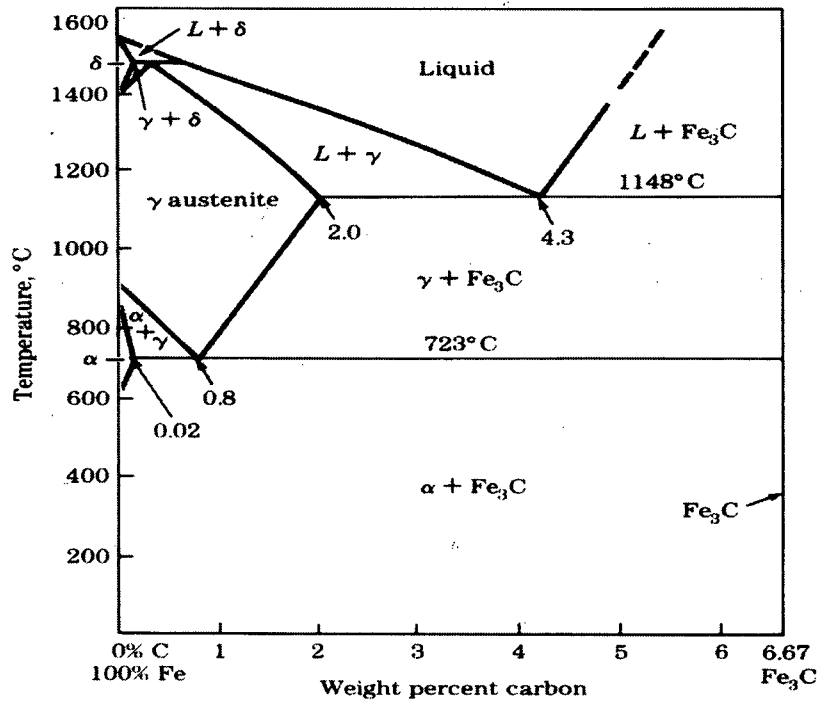


Figure 2-4 : Fe-Fe<sub>3</sub>C phase diagram [44].

Manganese expands the austenite phase field and depresses the  $A_{e3}$  and  $A_{e1}$  lines; thus it reduces the size of the intercritical ( $\alpha+\gamma$ ) region [46]. Therefore, a steel with a higher Mn content would be expected to form more austenite after intercritical annealing at a given temperature than a steel of the same carbon but lower Mn content. It is also known that Mn increases initial austenite content with reducing the carbon concentration of austenite [96].

On the other hand, Si hardly affects carbon concentration in austenite particles in the same manner as aluminum and chromium [97]. However, it is known that Si suppresses carbide precipitation and enhances the volume fraction of retained austenite [69]. During austempering, carbide precipitation is inhibited by the presence of Si which does not dissolve in carbide [69], and hence carbon content in retained austenite increases with increasing Si content, which is generally accompanied with increasing volume fraction of retained austenite [37, 48, 49].

The alloying elements Mn and Si also affect the kinetics of the phase transformations in the system. It is well known that Mn and Si in a plain carbon steel shift the TTT curve of pearlite transformation towards longer transformation times [55]. The bainite transformation start temperature,  $B_s$ , is greatly decreased by the presence of manganese, as indicated by the following empirical equation [56]:

$$B_s(^{\circ}\text{C}) = 830 - 270C - 90Mn - 37Ni - 70Cr - 83Mo \quad (2.4)$$

The martensite start temperature,  $M_s$ , is also affected by the addition of Mn and Si, as shown in the modified Andrews equation [18]

$$M_s(^{\circ}\text{C}) = 539 - 423C - 30.4Mn - 17.7Ni - 12.1Cr - 7.5Mo + 10Co - 7.5Si \quad (2.5)$$

For TRIP steels, it is critical to reduce  $M_s$  below room temperature and thereby stabilizing retained austenite. From the above equation, it can be seen that this is facilitated by the enrichment of carbon during the bainite tempering region.

#### ***2.1.4 Processing and Microstructure***

Multi-phase (DP and TRIP) steels can be produced as hot-rolled or as cold-rolled and annealed material [3]. Hot rolled multi-phase steels are obtained by controlled cooling during hot-rolling process. Cold rolled multi-phase steels, which are industrially more common, are obtained from a standard cold rolled ferrite-pearlite grade by a 2-stage heat treatment. Figure 2-5 shows schematically the intercritical annealing process and carbon enrichment for producing DP and TRIP steels. In the first part of the annealing treatment the material is annealed at an intercritical temperature (in the  $\alpha+\gamma$  range). During this annealing treatment, at a temperature between  $Ac_3$  and  $Ac_1$ , recrystallization of ferrite, dissolution of cementite, and the formation of austenite takes place [65, 66]. The amount of austenite formed depends on the annealing temperature. The key to the stabilization of a metastable residual austenite content in the structure is the carbon enrichment of the austenite [2]. Starting from an average carbon content of approximately 0.20 wt%, this is achieved in the two heat treatment stages. In the first step, the development of austenite is promoted by suitable forming and temperature conditions. Because virtually no carbon is

dissolved in the ferrite, a carbon enrichment of up to 0.5 wt% can be achieved independently of the ferrite content. At this time, if the strip is cooled rapidly to room temperature, the enriched austenite is then transformed into martensite which results in ferrite and martensite DP steel.

In contrast, TRIP steels are cooled in the next step to the temperature range of the bainite transformation. During fast cooling from intercritical annealing to the overaging region, transformation of austenite to pearlite is avoided. The intercritical annealing is followed by an isothermal tempering stage in the bainite transformation temperature range. During this tempering, part of the austenite transforms to bainite, whereas residual austenite may become sufficiently stabilized by carbon rejection from bainitic ferrite as to not transform to martensite during the final quenching to room temperature. Due to the presence of alloying elements such as Si, Al, and P, the precipitation of iron carbide which is usually accompanied by the bainite transformation is prevented and the carbon, from the austenite, which transforms to bainitic ferrite builds up in the remaining austenite[67, 68]. With the further increase in the carbon content of the residual austenite, the temperature for the development of martensite falls to values below room temperature. This austenite therefore remains as metastable austenite in which the carbon content is about 1.4-1.8 mass% [69].

Therefore, the microstructure of cold-rolled and intercritically annealed TRIP steel consists of a matrix of ferritic grains with a dispersion of grains of second phases, bainite and retained austenite, located at grain boundaries, as shown in Figure 2-6 [41].

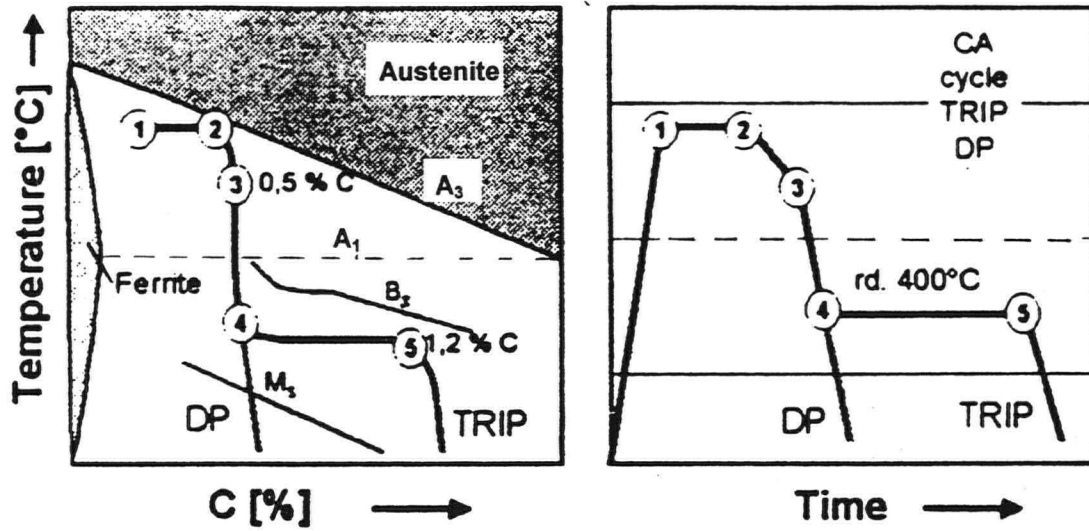


Figure 2-5 : Schematic drawing of the intercritical annealing process for producing DP and TRIP steels and carbon enrichment [2]

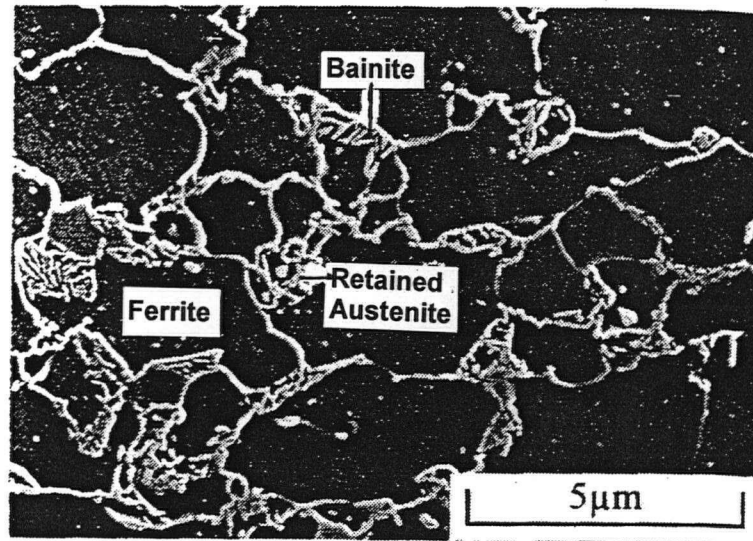


Figure 2-6 : SEM micrograph of the typical microstructure of the industrially produced TRIP steel [41]

## 2.2 Microstructural Aspects of Austenitization

There have been a number of papers published recently which deal with the mechanism of austenite formation starting from ferrite-pearlite microstructures [70-75]. The process of austenitization can be divided into three stages:

1. nucleation of austenite nodules at the interface between  $\alpha$  and  $\text{Fe}_3\text{C}$
2. growth of austenite
3. final equilibrium of ferrite and austenite

Speich *et al.*[71] have concluded that the first stage of austenite formation in 1.5 % Mn low carbon steels with ferrite-pearlite microstructure occurs by nucleation of austenite at the ferrite/pearlite interfaces and the subsequent growth of the austenite into pearlite until pearlite dissolution is complete. The kinetics of austenite formation are initially quite rapid and controlled by carbon diffusion, but later stages are quite sluggish and associated with the partitioning and diffusion of substitutional alloying elements, such as manganese [71, 76].

In pearlitic steels, there is a large interfacial area between  $\alpha$  and  $\text{Fe}_3\text{C}$ . As Figure 2-7 [77] illustrates, nucleation could conceivably occur either within a pearlite colony (site A), or at a colony boundary (site B), edge (site C), or corner (not shown). Because of the orientation

relationship which exists between adjacent plates of  $\alpha$  and  $\text{Fe}_3\text{C}$  within a pearlite colony [78], this is a relatively low energy interface, whereas the boundary between two or more colonies has a relatively high surface energy. Generally, then, it is boundary sites which have been confirmed as being the effective nucleation sites [79].

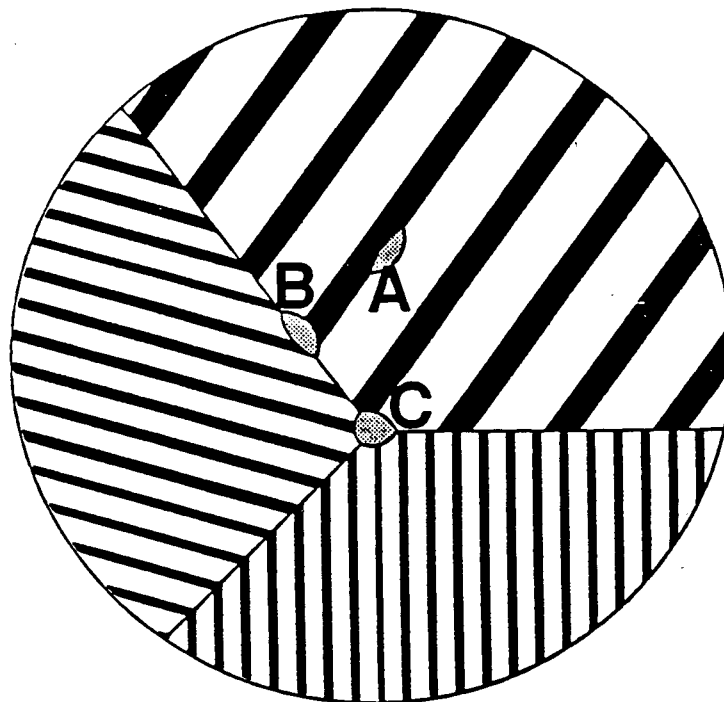


**Figure 2-7 : Potential austenite nucleation sites in a pearlitic microstructure: interlamellar (site A), colony boundary (site B), and colony edge (site C) [77]**

Garcia and DeArdo [72] performed austenitization tests with four steels, all containing approximately 1.5% Mn, and varying in carbon content from 0.01% to 0.22%. They found that in the primarily ferritic samples, austenite nucleated at  $\text{Fe}_3\text{C}$  particles located on ferrite grain boundaries. This was observed in both recrystallized and 70% cold worked samples. In samples containing a mixture of ferrite and pearlite, they observed that  $\gamma$  nucleation took place on  $\text{Fe}_3\text{C}$  particles which were located either on pearlite colony boundaries, or on boundaries between pearlite colonies and ferrite grains.

Yang et al. [80] found that  $\gamma$  nucleated first on boundaries between deformed and unrecrystallized ferrite grains, and then on spheroidized cementite particles in recrystallized ferrite. They also reported [73] that in a normalized ferritic-pearlitic microstructure, austenite nuclei generally form first at coarse carbide precipitates located at ferrite grain boundaries, and that austenite can also nucleate at carbide particles within a colony of spheroidized pearlite.

The  $\gamma$  nucleation in ferrite-pearlitic microstructures can be summarized such that the active  $\gamma$  nucleation site is an  $\alpha/\text{Fe}_3\text{C}$  interface located at a pearlite colony boundary, where excess surface energy exists to promote heterogeneous nucleation [50, 71, 72]. At this stage, however, dissolved pearlite regions transform only partially to austenite, remaining some

ferrite in the regions of the dissolved pearlite, without transforming to austenite [70]. This fact indicates that the dissolution rate of pearlite is faster than the growth rate of austenite.

The growth of the austenite phase constitutes a second step of austenitization. This step is sometimes divided into two or more stages [50, 70]. Souza et al. [50], for instance, observed that the first substage involves the transformation of pearlitic regions to austenite, during which the carbon from the dissolving pearlitic cementite seems to move simultaneously into the growing austenite, adjacent pearlitic ferrite, and ferrite surrounding pearlite. The growth rate of austenite in this stage is controlled primarily by the rate of carbon diffusion in austenite. Souza et al. [50] went on to show that subsequent growth of this austenite into matrix ferrite constitutes a second substage. The growth of the austenite in this stage may be controlled either by carbon diffusion in austenite or by manganese diffusion in ferrite.

In the third and final step, final equilibrium of ferrite and austenite is achieved. The growth process of austenite in this step is controlled by the diffusion of manganese in austenite [70, 71]. The manganese concentration gradients within the austenite will be eliminated by manganese diffusion through the austenite. However, this final step of austenitization will be very slow because the diffusion rate of manganese in austenite is five to six orders of magnitude lower than for carbon and three orders of magnitude slower than in ferrite [70].

## 2.3 Modeling of Austenitization

### 2.3.1 Avrami Equation

In order to describe phase transformation kinetics, several attempts have been made to employ empirical or semi-empirical equations [81- 84]. For example, the Avrami equation and the additivity rule were successfully applied to describe the  $\gamma \rightarrow \alpha$  and  $\gamma \rightarrow P$  transformations during continuous cooling of a 1025 carbon steel [82]. The empirical equations are often more useful to describe complex situations which occur under industrial processing conditions [84].

Johnson and Mehl [85], Avrami [86, 87] and Kolmogorov [88] were pioneers in the development of an equation to describe isothermal transformation kinetics. They suggested a general kinetic law for the case of homogeneous transformation, in which every small portion of untransformed material has the same probability of transforming in a given time. In this case, the rate of transformation will be proportional to the volume of material as yet untransformed. The fraction transformed is given by

$$X = 1 - \exp(-bt^n) \tag{2.6}$$

where  $X$  is the normalized fraction transformed,  $b$  and  $n$  are constants and  $t$  is the time at transformation temperature. This equation is known as the Johnson-Mehl-Avrami-Kolmogorov (JMAK) [85- 89] equation, or simply the Avrami equation. Broadly speaking,  $b$  is a rate constant reflecting the nucleation and/or growth rate, while  $n$  is dependent on the nucleation conditions and the dimensionality of the transformation, as summarized in Table 2.1 [90]. In the case of site saturation, Cahn [91] examined the effect of different nucleation sites on the exponent  $n$  and found that  $n = 1, 2$  and  $3$  are appropriate exponents for nucleation at grain boundaries, grain edges and grain corners, respectively.

**Table 2.1: Values of  $n$  in the Avrami equation [90]**

Conditions	nucleation and growth	nucleation with site saturation
1-dimensional growth	2	1
2-dimensional growth	3	2
3-dimensional growth	4	3

### 2.3.2 *The Principle of Additivity*

As noted by Christian [90], the treatment of non-isothermal transformations is considerably complicated by the fact that the rates of nucleation and growth usually vary independently with temperature. The problem can be simplified if the reaction is additive.

The additivity principle was originally proposed by Scheil [93] to predict the onset of transformation under a continuous cooling condition. It has since been extended to describe non-isothermal transformation kinetics from isothermal data.

It was proposed that the time spent at a particular temperature,  $\Delta t_i$ , divided by the isothermal time  $t_i$ , that is required to start the transformation at that temperature may be considered to represent the fraction of the total incubation (nucleation) time consumed at that temperature. Scheil [93] postulated that for a non-isothermal treatment, the transformation will start when the sum of the fractional incubation times equals unity. Mathematically, this may be expressed as

$$\sum_{i=1}^n \frac{\Delta t_i}{t_i} = 1 \quad (2.7)$$

where  $n$  is the number of incremental steps used in describing the non-isothermal heating event between the equilibrium temperature and the temperature at which transformation start is observed. Thus, the total time to reach the onset of transformation can be obtained by adding the fractional time increments to reach this stage isothermally, until the sum of the fractions reaches unity. A transformation of this kind is known as an additive reaction.

The generalization of Eq. (2.7) to any non-isothermal (heating or cooling) process is described as the principle of additivity expressed by Cahn [94] and Christian [92]

$$\int_0^1 \frac{dt}{t_a(T)} = 1 \quad (2.8)$$

in which the integral represents the summation of the fractional isothermal transformation times, where  $t_a(T)$  is the isothermal time to reach a specific fraction transformed.

It follows from this that a continuous heating or cooling transformation may be approximated as a series of short isothermal segments, as illustrated in Figure 2-8.

Essentially, the transformation is allowed to proceed isothermally, at  $T_1$ , for instance, for a short time interval,  $\Delta t$ . The temperature is then instantaneously changed, to  $T_2$ , and the transformation is continued again for a short time interval, and so on. At the start of each successive time step, a virtual time,  $t_v$ , may be calculated. The virtual time is the time required to reach the current fraction transformed,  $X$ , if the entire transformation had been carried out isothermally at that temperature. The overall effect is that of a stepwise approximation to the continuous transformation, as shown in Figure 2-9.

Cahn [94] examined the additivity principle with application to the transformation process. He expressed a criterion for specifying as additive reaction: "whenever the reaction rate is a

function of only the instantaneous temperature and the amount already transformed, the reaction may be considered additive;" i.e.,

$$\frac{dX}{dt} = f(X, T) \quad (2.9)$$

where  $\frac{dX}{dt}$  is the rate of change of fraction transforming,  $X$  is the fraction transformed and  $t$  and  $T$  are the transformation time and temperature, respectively. Christian [90] modified this criterion further and found that additivity will only be satisfied if the transformation rate can be described by

$$\frac{dX}{dt} = \frac{H(T)}{G(X)} \quad (2.10)$$

where  $H(T)$  and  $G(X)$  are functions only of temperature,  $T$ , and fraction transformed,  $X$ , respectively. An additive reaction thus implies that the reaction rate depends solely on the state of the assembly and not on the thermal path which leads to that state.

It can be shown that the Avrami equation (Eq. (2.6)) obeys the criterion proposed by Christian [90], if certain assumptions are made. Rearranging the Avrami equation (Eq. (2.6)):

$$t = \left\{ \ln \frac{(1-X)}{-b} \right\}^{1/n} \quad (2.11)$$

Differentiating Eq. (2.6) with respect to  $t$ ,

$$\frac{dX}{dt} = -\exp(-bt^n)(-nbt^{n-1}) \quad (2.12)$$

Substituting Eq. (2.11) into (2.12),

$$\frac{dX}{dt} = nb^{1/n} [-\ln(1-X)]^{\frac{n-1}{n}} (1-X) \quad (2.13)$$

Thus, if  $b$  is a function of temperature only and  $n$  is a constant, Eq. (2.13) satisfies Christian's equation (Eq. (2.10)).

Earlier, Avrami [86, 87, 89] defined an "isokinetic" range, in which the nucleation rate is proportional to the growth rate, over which a reaction would be additive. Under these conditions, the isothermal transformation results can be used to describe phenomena that take place under conditions of varying temperature.

Cahn [94] recognized that the isokinetic condition is a very special condition which is not commonly encountered in many transformations. He noted that in many systems, nucleation sites are rapidly exhausted early in the reaction and the subsequent transformation process is dominated by growth, which is a temperature-dependent parameter. He therefore generalized the idea by defining an isokinetic reaction as one in which

$$X = F \left[ \int h(T) dt \right] \quad (2.14)$$

where  $h(T)$  is a single function of temperature. The consequence of Eq.(2.14) is that a reaction in which the nucleation and growth rates vary independently is not, in general, expected to be additive. If, however, the nucleation sites are saturated early in the reaction, then the transformation subsequently depends only on the growth rate of pre-existing nuclei. Cahn termed this situation “site saturation”, and stated that such a transformation would be additive.

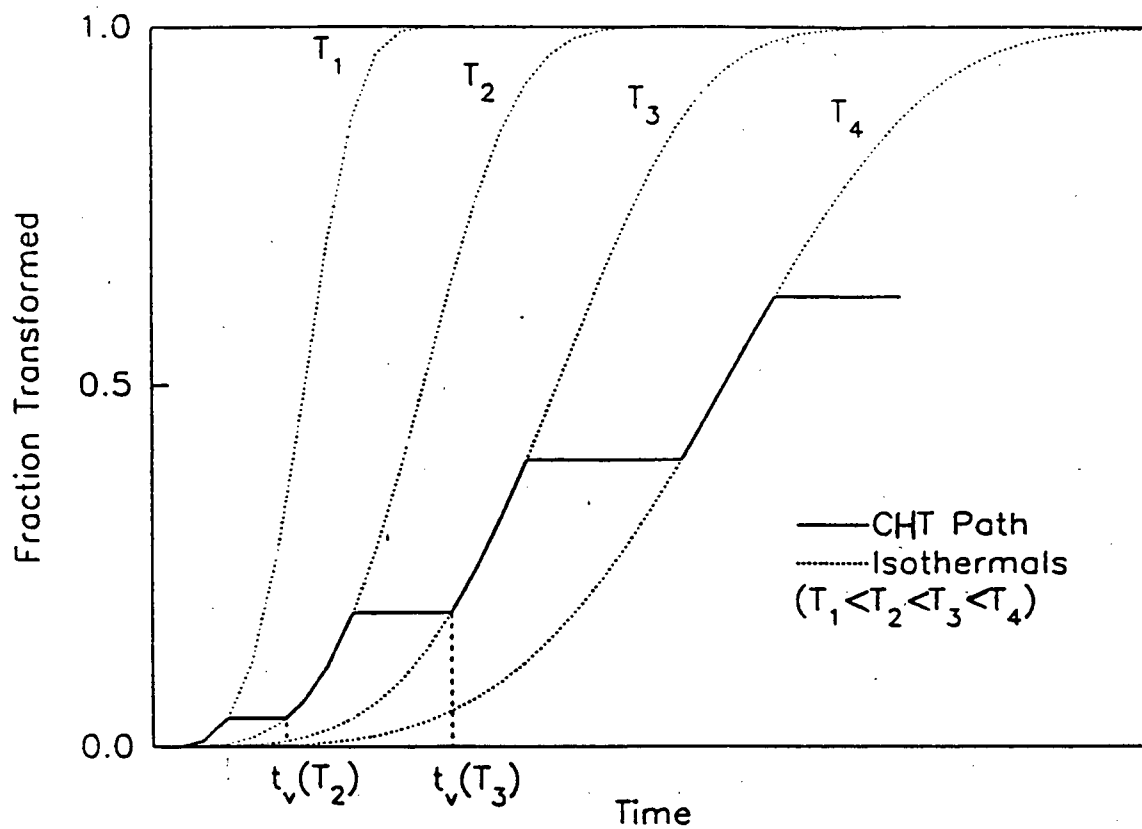
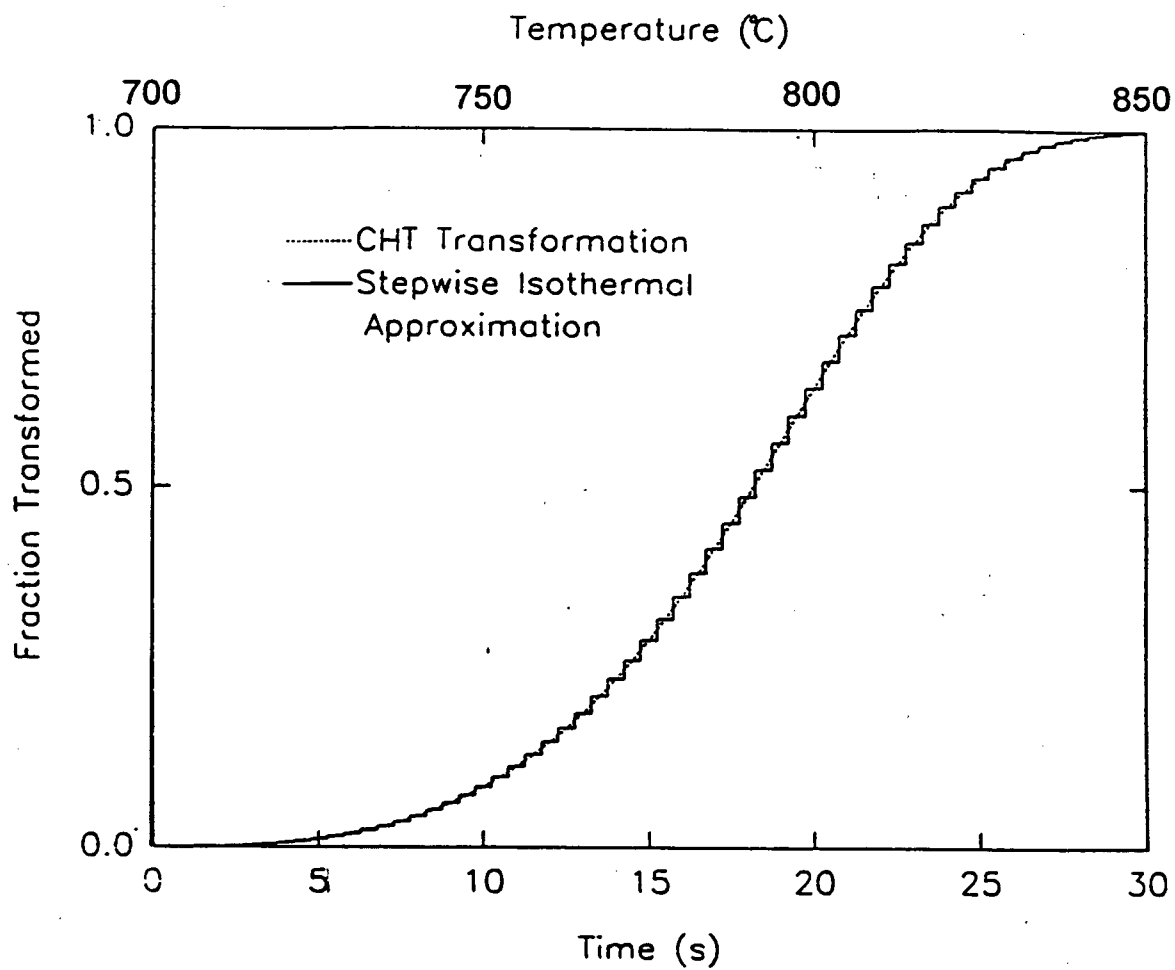


Figure 2-8 : Schematic illustration of the use of the additivity principle for the prediction of continuous heating kinetics, showing a series of isothermal transformation curves and their relationship to a stepped transformation event [77]



**Figure 2-9 : Diagram showing the approximation of continuous heating kinetics as the sum of a series of short duration isothermal increments [77]**

### 2.3.3 Diffusion Model

Carbon diffusion in austenite as the rate determining step has been used in a number of austenite growth models [9, 10, 44, 71, 95]. In order to describe the austenite growth kinetics from pearlite/ferrite mixture, it is usually assumed that there is local equilibrium at the pearlite/austenite (P/ $\gamma$ ) and ferrite/austenite ( $\alpha/\gamma$ ) phase boundaries. Then the process is divided into two steps. The first step consists of pearlite dissolution and growth of austenite into pearlite at a rate controlled primarily by carbon diffusion in austenite with the diffusion path lying along the pearlite/austenite interface [71]. By using a simple one-dimensional slab model and assuming instantaneous nucleation of austenite as a thin film at the ferrite/pearlite interface and growth inward, the time for complete dissolution of the pearlite,  $t_p$ , is given simply by [71]

$$t_p = a/G \quad (2.15)$$

where  $a$  is the half-thickness of the pearlite slab and  $G$  is the growth rate. If only one pearlite slab is assumed to occupy each ferrite grain, the value of  $a$  is given by

$$a = V_v(P)d/2 \quad (2.16)$$

where  $V_v(P)$  is the volume fraction of pearlite and  $d$  is the diameter of the ferrite grain.

The second step consists of the ferrite-to-austenite transformation. Assuming the process is only governed by the diffusion of carbon in austenite, the kinetics can be described by the following equations [47].

$$\frac{\partial C_v}{\partial t} = \frac{1}{x^m} \frac{\partial}{\partial x} \left( x^m D_v \frac{\partial C_v}{\partial x} \right) \quad v = \begin{cases} \alpha & \text{for } x \in [0, s(t)] \\ \gamma & \text{for } x \in [s(t), L] \end{cases} \quad (2.17)$$

$$v_n (C_\alpha^* - C_\gamma^*) = D_\gamma \left( \frac{\partial C_\gamma}{\partial x} \right)^* - D_\alpha \left( \frac{\partial C_\alpha}{\partial x} \right)^* \quad \text{for } x = s(t) \quad (2.18)$$

where  $t$  is time,  $C_v$  is the carbon concentration in the phase  $v$  ( $\alpha$  or  $\gamma$ ),  $D_v$  is the associated diffusion coefficient,  $x$  is location and  $s(t)$  is the position of the  $\alpha/\gamma$  interface (see Figure 2-10),  $v_n$  is the normal velocity of the  $\alpha/\gamma$  interface,  $C_\alpha^*$  and  $C_\gamma^*$  are the concentrations at the interface in the  $\alpha$  and  $\gamma$  domains, respectively. The symbol  $*$  denotes values taken at the interface. The geometry parameter  $m$  is equal to 0, 1 or 2 for the planar, cylindrical and spherical geometries, respectively.

The boundary conditions at the external boundary of the domain and the initial conditions are given by:

$$\frac{\partial C_v}{\partial x} = 0 \quad x = 0, L \quad (2.19)$$

$$C(x,0) = \begin{cases} C_\alpha(T_i) : \text{for } x \in [0, s(t)] \\ C_\gamma(T_i) : \text{for } x \in [s(t), L] \end{cases} \quad (2.20)$$

Eq.(2.17) through (2.20) are then solved by using the finite difference method. The details can be found in the literature [44].

Jacot et al. [95] satisfactorily applied the diffusion model to describe the reaustenitization of ferrite-pearlitic plain carbon steel. In their study, the diffusion model was coupled with a Monte Carlo simulation. The diffusion model was used to describe the ferrite-to-austenite transformation. While the Monte Carlo model was applied to simulate grain growth in austenite.

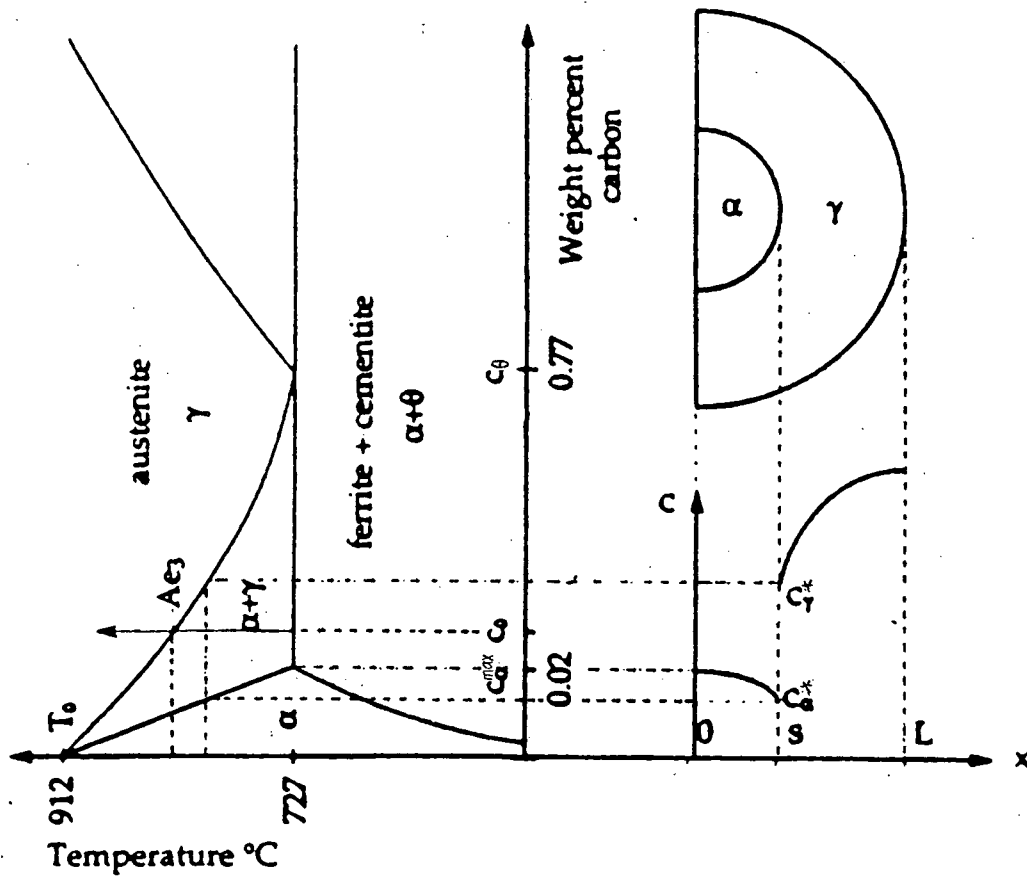


Figure 2-10 : Representation of the one-dimensional domain  $[0, L]$  (spherical geometry), of the solute profiles in the  $\alpha$  and  $\gamma$  regions and the corresponding equilibrium phase diagram [44].

## **CHAPTER 3 – EXPERIMENTAL WORK**

### **3.1 Materials**

All experimental work was conducted with a low plain-carbon steel having the composition shown in Table 3.1. This steel was provided by STELCO Inc. as hot-rolled plates with ferrite-pearlite microstructure. In order to obtain different starting microstructures, the hot plates were separated into two groups. The first group was remained as hot rolled (as-received) material and the second group was further cold rolled to 20% and 50% reduction, respectively, in the pilot mill of CANMET in Ottawa. Specimens for the continuous heating tests (CHT) were machined from these two groups of material. In addition, some specimens of the first group were in-situ heat treated in the dilatometer chamber to produce a fully bainitic structure before CHT. Specimens were heated at a rate of 10°C/s to 1000°C and held for one minute, then helium quenched to 500°C, and then slowly cooled to room temperature at 3°C/s. Consequently, the continuous heating tests were conducted with four different starting microstructures – hot rolled (HR), bainitic (Bainite), 20% cold rolled (20CR) and 50% cold rolled (50CR).

**Table 3.1: Chemical compositions (in wt. %) of the steel investigated.**

<b>C</b>	<b>Mn</b>	<b>Si</b>	<b>P</b>	<b>S</b>	<b>Al</b>	<b>Cr</b>	<b>Ni</b>
0.16	1.38	0.24	0.008	0.011	0.045	0.03	0.005
<b>Cu</b>	<b>Mo</b>	<b>V</b>	<b>Nb</b>	<b>Ti</b>	<b>Sn</b>	<b>N</b>	<b>ASA</b>
0.01	0.006	0.003	0.002	0.002	0.002	0.004	0.043

## 3.2 Experimental Techniques

### 3.2.1 Continuous Heating Tests

Table 3.2 shows the experimental conditions of continuous heating tests. Samples were brought to 600°C at 10°C/s and then continuously heated above the  $A_{c3}$  temperature to 950°C at heating rates which varied from 0.3°C/s to 300°C/s.

**Table 3.2: Experimental conditions of continuous heating tests**

Specimen		Microstructure	Heating Rate (°C/s)
<b>HR</b>	Hot Rolled	$\alpha$ +Pearlite	0.3, 1.0, 10 30, 100, 300
<b>Bainite</b>	Bainitic	bainite	
<b>20CR</b>	20% Cold Rolled	$\alpha$ +Pearlite	
<b>50CR</b>	50% Cold Rolled	$\alpha$ +Pearlite	

The continuous heating tests were performed using a Gleeble 1500 Thermomechanical Simulator, equipped with a dilatometer to record the transformation kinetics.

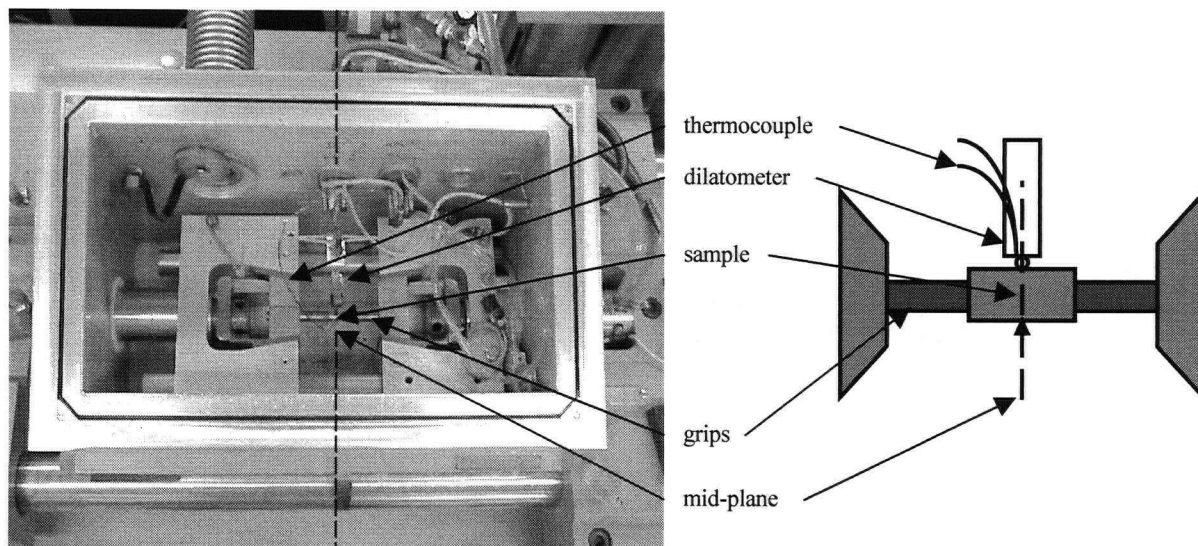
The specimen chamber of the Gleeble and the basic component of the chamber are shown in Figure 3-1. The Gleeble is equipped with a sealed chamber, inside which samples of various shapes and sizes can be resistively heated and gas or water quenched.

Figure 3-2 shows the specimen design used in the CHT experiments. A thin-walled tubular specimen, with dimensions of 8 mm (6 mm for the 50CR specimen in Table 3.2) outer diameter, 1 mm wall thickness by 20 mm length, to minimize radial temperature gradient. The temperature of the specimen was controlled and monitored using an intrinsic Chromel-Alumel thermocouple which was spot welded onto the outer surface of the specimen at mid-length, the plane of the dilatometer position, as shown in Figure 3-2.

The kinetics of  $P \rightarrow \gamma$  and  $\alpha \rightarrow \gamma$  phase transformations, which involve volume changes due to the transition from a bcc to a fcc crystal structures, are measured continuously by a Linear Variable Differential Transformer (LVDT) diametral and longitudinal strain measuring device. In order to minimize oxidation during the experiment, the dilatometer chamber was evacuated to a pressure of less than 3 mTorr and back filled with argon gas. This procedure was repeated before each test commenced.

During each test, the time, programmed temperature, measured temperature, and dilatometer output were measured and recorded continuously.

Figure 3-3 illustrates an example of a dilation measurement as a function of temperature for the continuous heating test for the HR material with a 1°C/s heating rate. At the temperatures above 820°C and below 720°C, the diameter of the specimen increases linearly with temperature. The slopes of the linear extension regions correspond to the thermal expansion coefficients of austenite ( $\alpha_\gamma$ ) and the initial structure which is a combination of ferrite and pearlite ( $\alpha_\alpha$ ), respectively. The region between these two linear sections represents the  $\alpha+P \rightarrow \gamma$  transformation. During the transformation, the dilation curve shows a decrease due to the atomic volume contraction associated with the crystal structure changes between  $\alpha$  (bcc) and  $\gamma$  (fcc). For this heating rate, the  $\alpha+P \rightarrow \gamma$  transformation starts at approximately 720°C and completes at temperature about 820°C. Figure 3-3 also indicates that after the  $P \rightarrow \gamma$  transformation is completed, the  $\alpha \rightarrow \gamma$  transformation is initiated. At higher heating rates, both transformations can be more vividly separated from the dilatometric response which will be shown in Chapter 4.



**Figure 3-1 : The specimen chamber and basic components of the Gleeble 1500 Thermomechanical simulator [98]**

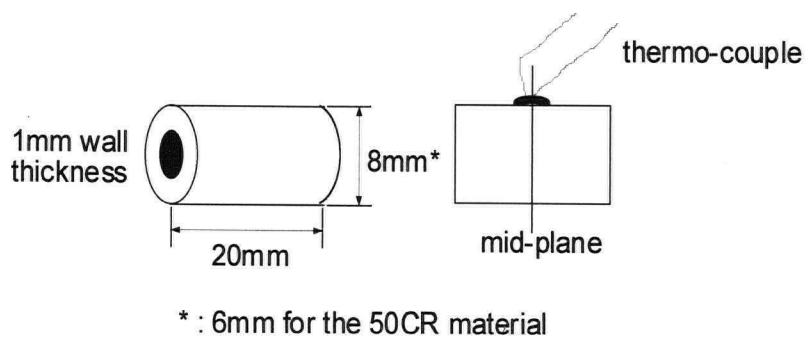


**Figure 3-2 : The specimen design for the Gleeble used in the CHT experiments**

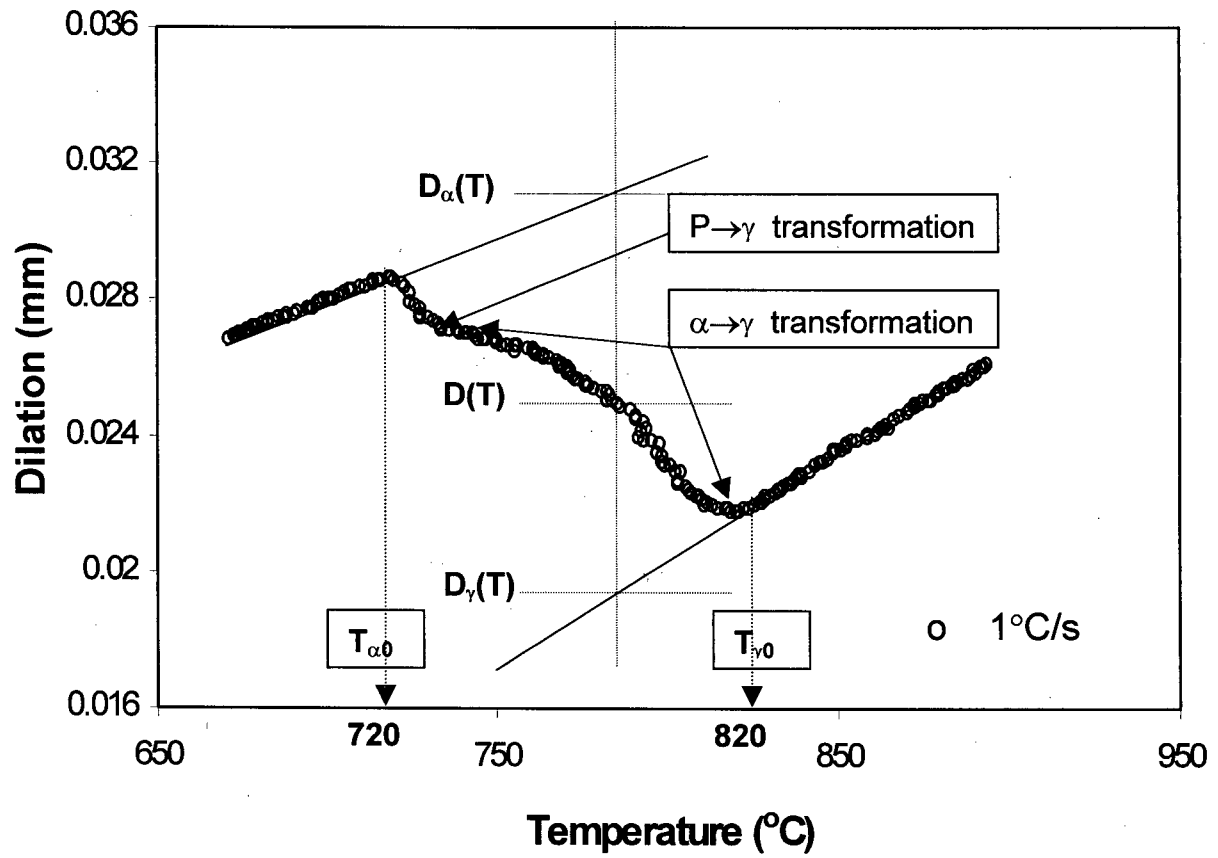


Figure 3-3 : Experimental dilation versus temperature results for a continuous heating test conducted at 1°C/s for the HR specimen. The solid lines indicate the extrapolations from the pre- and post-transformation regions.

The volume fraction of austenite formed,  $X_\gamma(T)$ , was determined from the dilation response,  $D(T)$ , as follows [51, 52]:

$$X_\gamma(T) = \frac{D_\alpha(T) - D(T)}{D_\alpha - D_\gamma} \quad (3.1)$$

where

$$D_\alpha = D_\alpha(T_{\alpha 0}) + \alpha_\alpha(T - T_{\alpha 0}) \quad (3.2)$$

and

$$D_\gamma = D_\gamma(T_{\gamma 0}) + \alpha_\gamma(T - T_{\gamma 0}) \quad (3.3)$$

are the extrapolated dilations from the untransformed and fully transformed regions, with  $T_{\alpha 0}$  and  $T_{\gamma 0}$  being limiting temperatures within these two regions, and  $\alpha_\alpha$  and  $\alpha_\gamma$  are the thermal expansion coefficients of ferrite-pearlite mixture and austenite phases, respectively.

The transformation start and finish time and temperatures were taken to be the points of 5% and 95% transformed, respectively. Eq. (3.1) is consistent with the assumption of a law of mixtures for the thermal expansion coefficient,  $\alpha_{mix}$ , during the transformation, i.e.:

$$\alpha_{mix} = \alpha_{\alpha} X + \alpha_{\gamma} (1 - X) \quad (3.4)$$

where  $X$  is the volume fraction transformed.

### **3.2.2 Microstructural Investigation**

A number of samples were helium quenched part way through the transformation, and then mounted and polished for metallographic examination. This was done for two purposes: first, to verify the fraction transformed concluded from dilation measurements, and second, to provide microstructural detail on the reversion kinetics mechanism.

Specimens, including those to characterize the initial structures, for metallographic examination were cut from the mid-length where the thermocouple was spot welded, using an  $\text{Al}_2\text{O}_3$  cut-off wheel. A directed spray coolant was used to protect the specimens from overheating during cutting. After cutting, one half of the sample from the thermocouple

position was cold mounted in a resin polymer and then ground progressively using 120 through 600 grit silicon carbide papers and finally polished employing a 6  $\mu\text{m}$  and a 1  $\mu\text{m}$  diamond solution.

Both optical and scanning electron microscopy (SEM) were applied for the metallographic evaluation of the specimens. For the optical microscopy, 2% nital (2 vol.% of nitric acid + 98 vol.% of methanol) was used as an etchant for approximately 7-10 seconds. This was found to etch samples more deeply than required for SEM observation. Thus, SEM samples to check the interlamellar spacing of pearlite were etched lightly in 1% nital.

Quantitative analysis of the microstructure was carried out in cross-section utilizing a C-Imaging System image analyzer, the ferrite grain size and ferrite fraction being quantified. The polished and etched specimens were photographed either using the CCD camera of the imaging system or a basic black and white optical microscope at magnification of  $\times 500$ . The microstructures were then traced on transparency film using a felt tipped pen for subsequent quantitative image analysis of ferrite grain size.

The ferrite grain size was quantified using Jeffries' method [92]. In this method, each whole grain was counted once and each partial grain, cut by the edge of the field of measurement, was counted as a half grain, as described by ASTM standard E112- 88 [92]. Knowing the number of grains for each field of interest, it was possible to determine the

mean equivalent area diameter (EQAD) grain size, in  $\mu\text{m}$ , by dividing the total area of the field of interest by the number of ferrite grains. To obtain statistically relevant results, at least 50 fields were quantified for the ferrite fraction and at least 500 ferrite grains were analyzed for the mean ferrite grain size.

In the SEM analysis, five to seven photomicrographs are taken of random locations on a polished and etched sample which contain, on average, approximately 10 pearlite colonies. Then, each interlamellar spacing measurements was averaged.

### ***3.2.3 Microhardness Measurements***

To supplement the metallographic investigation in particular for the CR materials where recovery and recrystallization may take place, microhardness measurements were conducted. A Beuhler Microhardness tester was used with a diamond Vickers indenter, 50g load, and 10s dwell time. At least ten measurements were taken for each sample and averaged to determine the hardness of the specimen and the hardness variability (standard deviation) throughout the specimen. All measurements are given according to the Vickers (HV) scale.

## **CHAPTER 4 – RESULTS AND DISCUSSION**

### **4.1 Initial Microstructures**

The starting microstructures of the four different materials are shown in Figure 4-1 (a) through (d). HR, 20% CR, and 50% CR materials consist of ferrite-pearlite aggregate microstructures, and the heat treated one is a fully bainitic structure.

The as-received HR material exhibits some banded regions. Their effect will be discussed later in section 4.2. In the case of the CR materials it can be seen that the grains were flattened and elongated during the cold rolling process. The bainitic structure shows a very fine mixture of ferrite and iron carbide as can be seen in Figure 4-1(b).

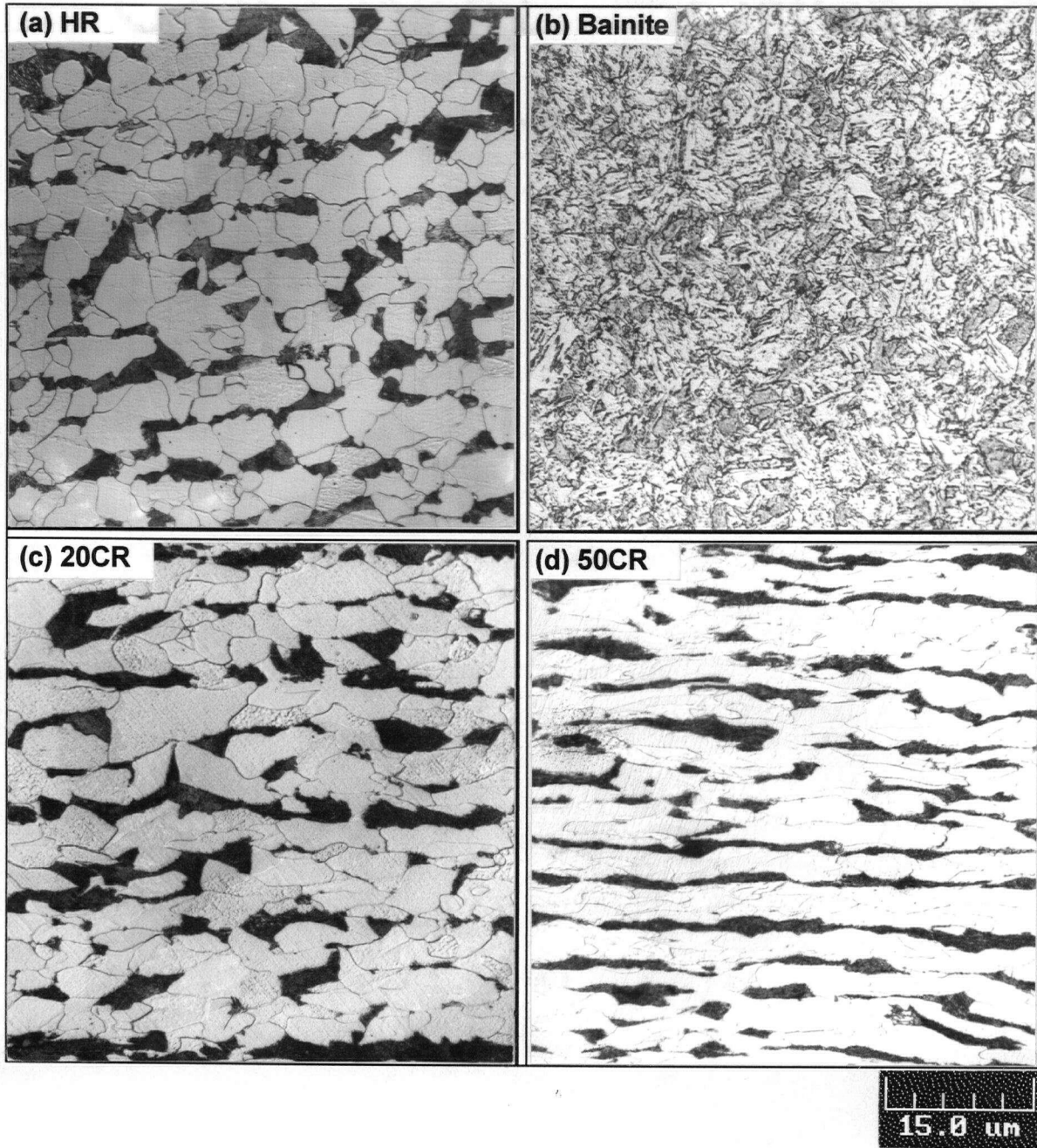


Figure 4-1 : Optical micrographs of starting microstructures (nital etch)

The initial microstructures were characterized in terms of the mean ferrite grain size, pearlite volume fraction, and the average pearlite spacing for the specimen HR, 20CR, and 50CR. The initial ferrite grain size of the HR material is approximately 10 $\mu$ m. The volume percent pearlite in the HR and CR materials is 18%. The pearlite spacings for HR, 20CR, 50CR materials are 0.20, 0.19, and 0.17 $\mu$ m, respectively.

## **4.2 CHT Data Analysis**

The continuous heating tests (CHT) were performed on a Gléeble 1500 Thermomechanical Simulator which was described in section 3.2.1. In order to obtain statistically relevant results, the continuous heating tests were repeated 4 to 11 times depending on the heating rates, which varied from 0.3°C/s to 100°C/s. However, it proved difficult to obtain reasonable consistency since the resulting dilation curves for most heating rates revealed some variation.

Figure 4-2 shows a typical variation of the curves plotted as the fraction transformed vs. temperature for the HR material with a 30°C/s heating rate. The variation of these test results is attributed to the following reasons. Probably the most plausible reason could be

the specimen conditions, i.e., the specimen dimension and the initial microstructure. The deviation of specimen dimension could cause the mismeasurement of the dilation change during the phase transformation. Another reason could be the initial microstructure, which contained some banded regions. This banding might have a pronounced effect on the nucleation of austenite, in that the banded region could be the preferential nucleation site of the austenite due to its high free energy. The stability of the dilatometer machine could be another reason for these variations.

Consequently, the data analysis for these transformation curves became a crucial part for this study. Two steps were employed to characterize the continuous heating transformation data:

1. accept experimental data based on selection criteria
2. averaging the accepted dilation data for a given heating rate

The first step for the data analysis was to accept a test to be successful. The transformation curves were selected only if the data satisfied both of the following conditions:

- (1) dilation data which have the thermal expansion coefficient ratio of 1.3~1.6 between ferrite and austenite, i.e.,  $\alpha_\gamma / \alpha_\alpha = 1.3 \sim 1.6$
- (2) dilation curves showing the total volume change ( $\Delta V/V$ ) of 0.9~1.6% at 800°C, which is equivalent to the dilation change ( $\Delta D/D$ ) of 0.003~0.005.

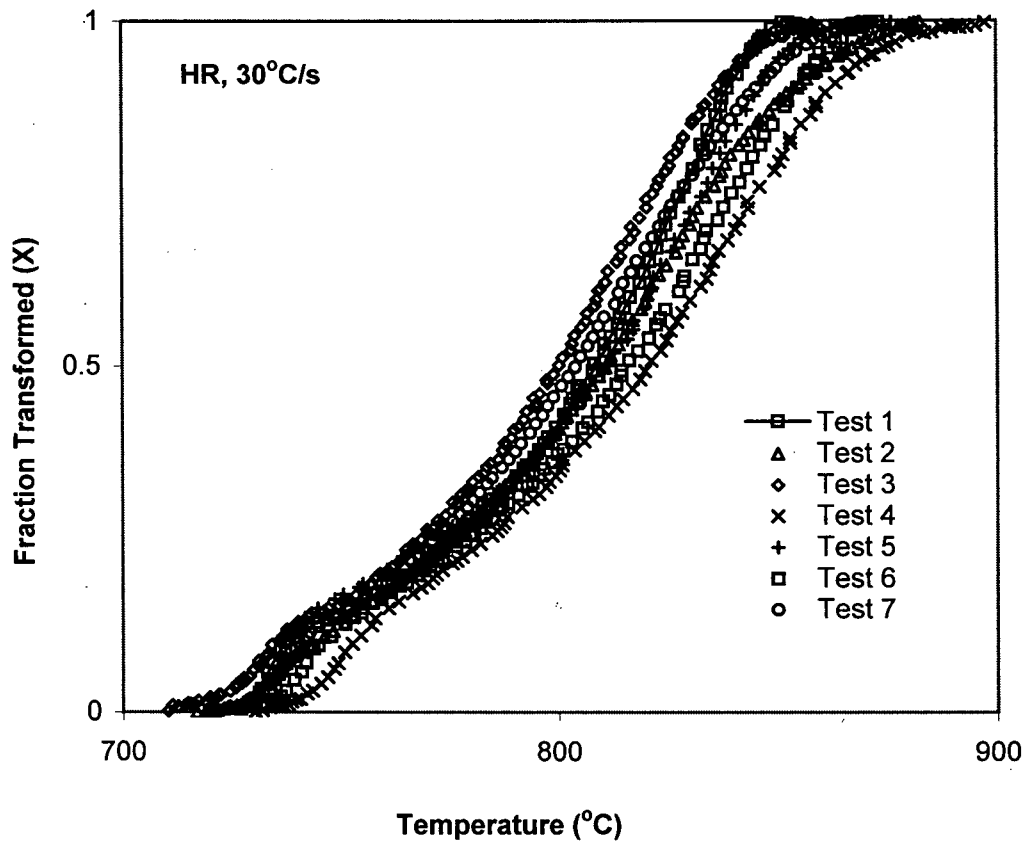


**Figure 4-2 : The austenite fraction vs. temperature curves showing a typical variation of transformation kinetics [HR material, 30°C/s]**

The thermal expansion ratio was based on the values of  $\alpha_\alpha=1.424\times 10^{-5}\text{K}^{-1}$  and  $\alpha_\gamma=2.065\times 10^{-5}\text{K}^{-1}$  [53] for ferrite and austenite, respectively, suggesting a ratio,  $\alpha_\gamma/\alpha_\alpha$ , of 1.45.

During the phase transformation at the temperature range of 710~820°C, there is approximately 1.2~1.4% volume contraction associated with the crystal structure changes from ferrite (bcc) to austenite (fcc). Assuming that the sample expands isotropically, the change of the sample diameter  $\Delta D$  referred to the initial diameter  $D_o$  at room temperature is related to volume change  $\Delta V$  and initial volume  $V_o$  at room temperature for small changes as follows [101]:

$$\frac{\Delta D}{D_o} = \frac{1}{3} \frac{V - V_o}{V_o} \quad (4.1)$$

Therefore,  $(\Delta D/D_o)$  can be calculated from the volumes of the unit cells at a certain temperature during continuous heating. For example, the total volume change associated with the  $\alpha \rightarrow \gamma$  transformation at 800°C is approximately 1.3% and this can be converted to dilation change  $(\Delta D/D_o)$  of 0.004 between these two phases.

Figure 4-3 shows an example of the data analysis for the HR material with a heating rate of 30°C/s. The dilation data for each CHT test are summarized in Table 4.1. Figure 4-3(a) illustrates the concepts of the two criteria for data selection. Subsequently, test 1 with  $\alpha_\gamma/\alpha_\alpha$

= 1.66 in Figure 4-3 (b) was removed based on the criterion of thermal expansion coefficient ratio, 1.3~1.6. Tests 4 and 5 were excluded because they exceed the criterion of the dilation change of 0.003~0.005. With other words, out of 7 tests only tests 2, 3, 6, 7 were accepted.

**Table 4.1 : Dilation data of the HR material with a 30°C/s heating rate**

Data	$\alpha_\gamma / \alpha_\alpha$	$\Delta D / D_0$
Test 1	1.66	0.004
Test 2	1.53	0.005
Test 3	1.36	0.004
Test 4	1.46	0.006
Test 5	1.51	0.007
Test 6	1.34	0.004
Test 7	1.32	0.005

Further data analysis for the dilation results was conducted by fitting the transformation curves with mathematical equations. In this study, there were two main stages to adopt the curve-fitting method. In general all transformation curves from the ferrite-pearlite initial structures showed a distinct  $P \rightarrow \gamma$  region followed by the  $\alpha \rightarrow \gamma$  transformation region. Therefore, the first stage was to divide the whole kinetic curve of the  $P + \alpha \rightarrow \gamma$  transformation into two separate curves, i.e.,  $P \rightarrow \gamma$  and  $\alpha \rightarrow \gamma$  transformations. The second stage was to derive the averaged transformation curve for each heating rate.

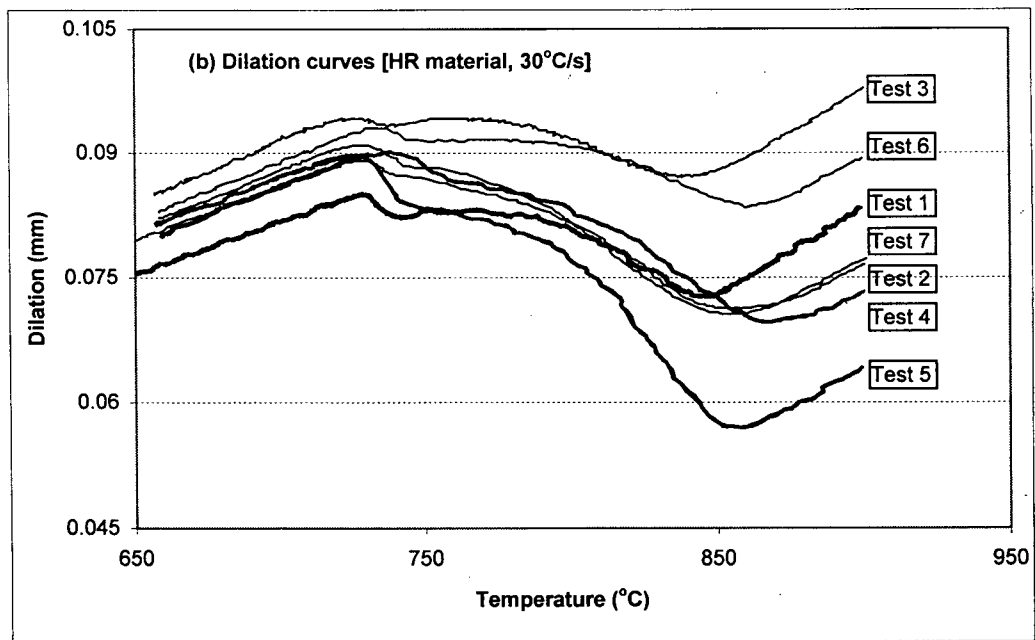
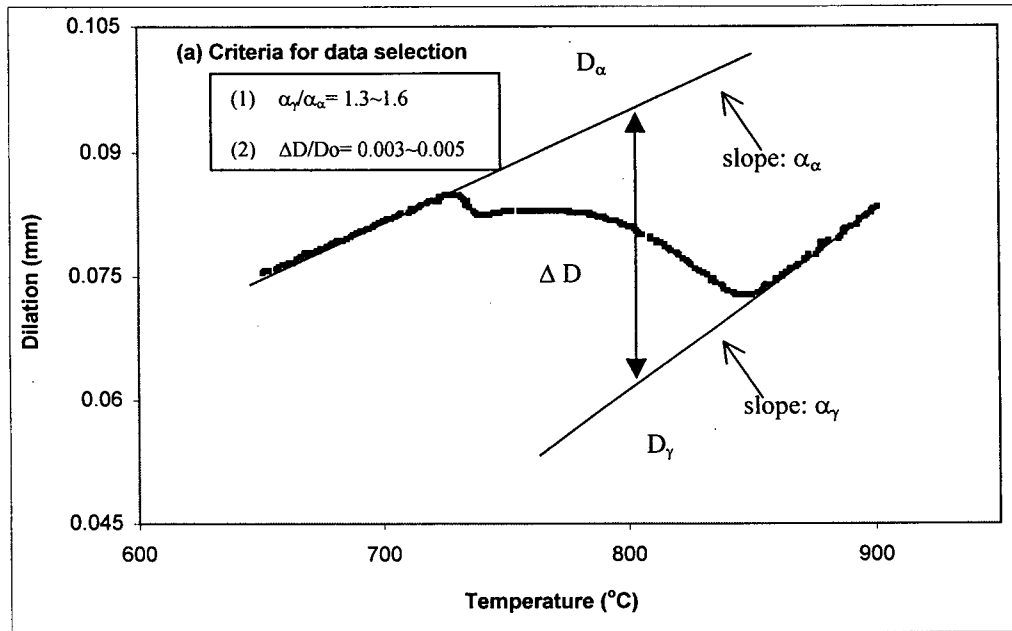


Figure 4-3 : Example of Data Analysis [HR material, 30°C/s]; (a) criteria for data selection, (b) dilation vs. temperature curves

Figure 4-4 shows examples of the curve fitting, highlighting the excellent agreement between the experimental and the fitting results. The following equations were used for this curve fitting.

$$Y_1 = P_i \{1 - \exp[-\exp(b_1 x^{e_1}) \exp(d_1 x^{e_1})]\} \text{ for } P \rightarrow \gamma \quad (4.2)$$

$$Y_2 = F_i \{1 - \exp[-\exp(b_2 x^{e_2}) \exp(d_2 x^{e_2})]\} \text{ for } \alpha \rightarrow \gamma \quad (4.3)$$

where  $Y_1$ ,  $Y_2$  are austenite fraction transformed from pearlite and ferrite,  $P_i$  (=0.18) and  $F_i$  (=0.82) are the initial volume fraction of pearlite and ferrite, respectively, and  $b_1 \sim e_2$  are fitting parameters.

Considering that the  $P+\alpha \rightarrow \gamma$  transformation starts from the pearlite portion, the curve-fitting was conducted firstly for the  $P \rightarrow \gamma$  portion (Eq. 4.2), followed by the  $\alpha \rightarrow \gamma$  portion (Eq. 4.3). After that, the mathematically expressed experimental curves were taken to derive the averaged transformation curve for each heating rate. As an example, Figure 4-5 summarizes the averaging procedure for 30°C/s heating rate of the HR material. The same procedure was followed to derive the averaged transformation curves for each heating rate of all three initially ferrite-pearlite materials, HR, 20CR, and 50CR.

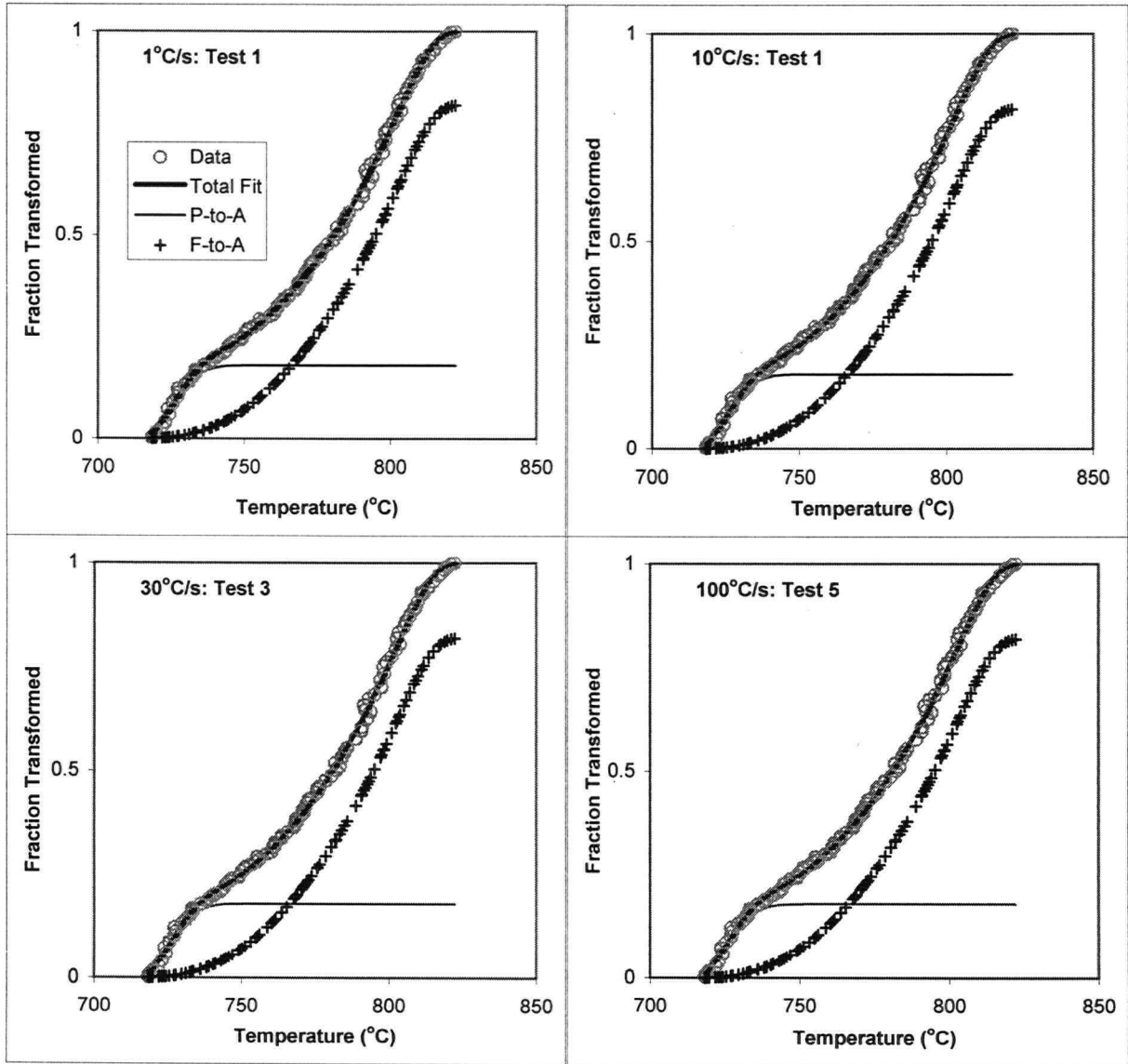


**Figure 4-4 : Examples of the curve fitting for the HR material in which the total transformation curves are divided into two separate curves, i.e.,  $P \rightarrow \gamma$  and  $\alpha \rightarrow \gamma$**

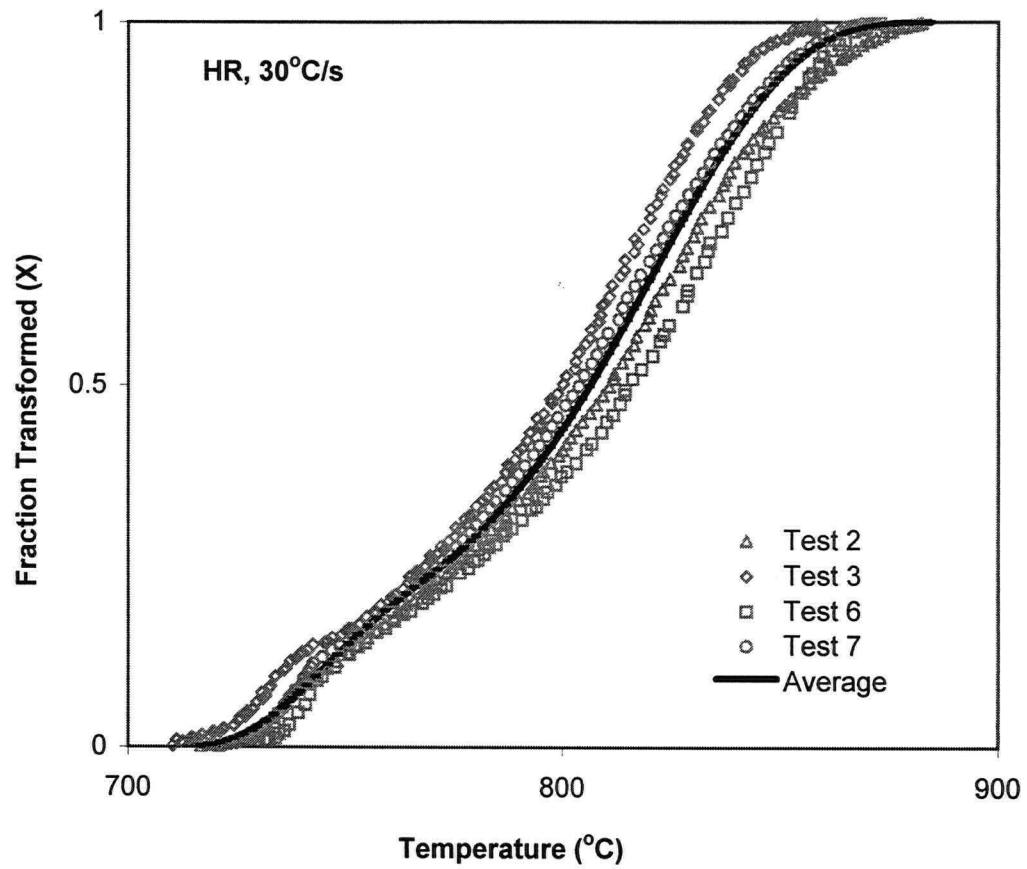


**Figure 4-5 : The averaged transformation curve for 30°C/s heating rate of the HR material.**

### 4.3 Effect of Heating Rate

The heating rate can have a pronounced effect on the phase transformation kinetics of these steels since increasing the heating rate requires higher superheating for the transformation to occur. Figure 4-6 displays the fraction transformed vs. temperature plot for the four initial materials. It can be clearly seen that as heating rate increases the transformation start and finish temperatures,  $T_S$  and  $T_F$ , increase. Considering  $1^\circ\text{C/s}$  and  $100^\circ\text{C/s}$  for the HR material, for example, the higher heating rate increases  $T_S$  and  $T_F$  by approximately  $20^\circ\text{C}$  and  $50^\circ\text{C}$ , respectively, as can be seen in Figure 4-7. This result is as expected and similar trends have been found for both the HR and CR materials but not for the Bainite material where no effect of heating rate is documented. The Bainite material, which consists of a very fine mixture of ferrite and carbide, provides a sufficiently high nuclei density such that the heating rate effect on the transformations is eliminated. As a result,  $T_S$  and  $T_F$  remain almost constant, regardless of the heating rates, as shown in Figure 4-7. Further, the diffusion distances are short and hence the transformation is very rapid.

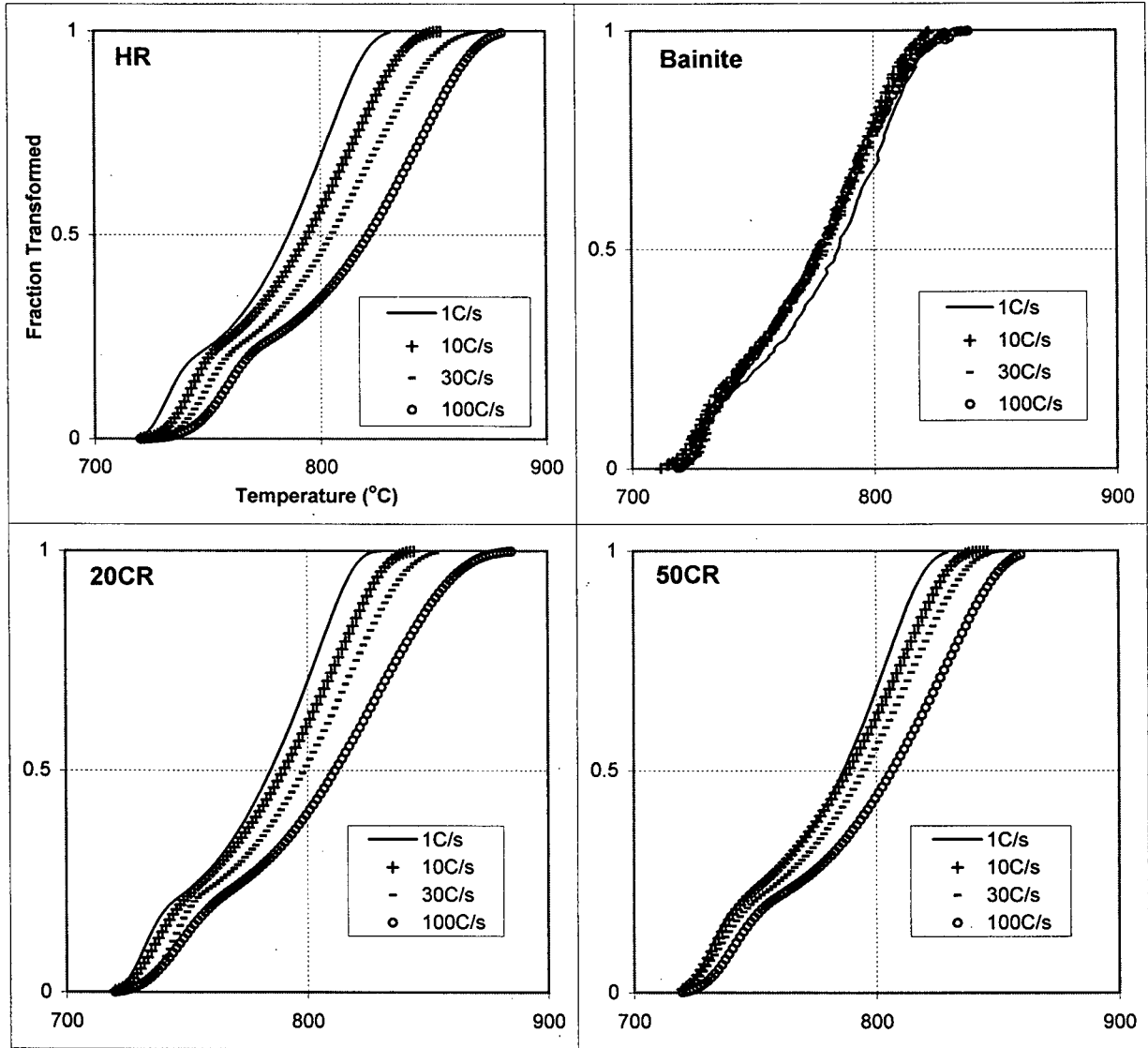


**Figure 4-6 : Effect of heating rate on continuous heating kinetics.**

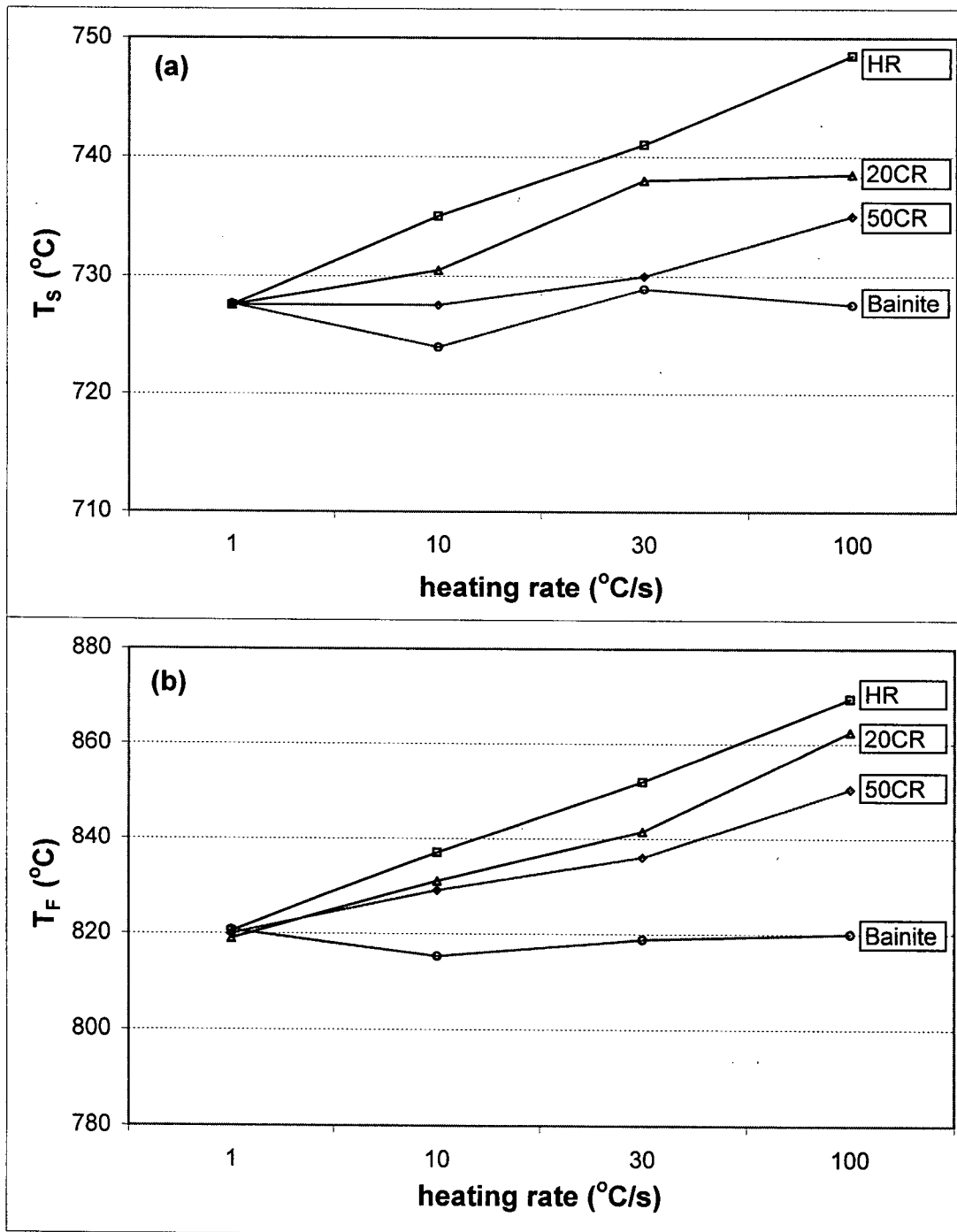


Figure 4-7 :  $T_S$  and  $T_F$  temperatures as a function of heating rates for different initial structures; (a)  $T_S$  and (b)  $T_F$

Considering the degree of heating rate effect between the HR and CR materials, however, it can be seen that the CR materials, especially the 50CR material, are less affected by the heating rates compared to the HR material. This is reflected by the fact that cold rolling elongates ferrite grains and fragments pearlite lamellae, thus increasing the number of sites of austenite formation during heating and thereby reducing the required superheating for the transformation to occur.

All curves show an initially rapid transformation of the pearlite portion preceding the  $\alpha \rightarrow \gamma$  transformation. Figure 4-8 shows the times for 5% and 95% transformation for the separated  $P \rightarrow \gamma$  and  $\alpha \rightarrow \gamma$  reactions for the HR material, respectively. It can be noticed here that pearlite transformation into austenite almost finishes, whereas the dissolution of ferrite to austenite has just started. This trend indicates that the austenite formation starts from the dissolved pearlite region and then the austenite grows into the ferrite.

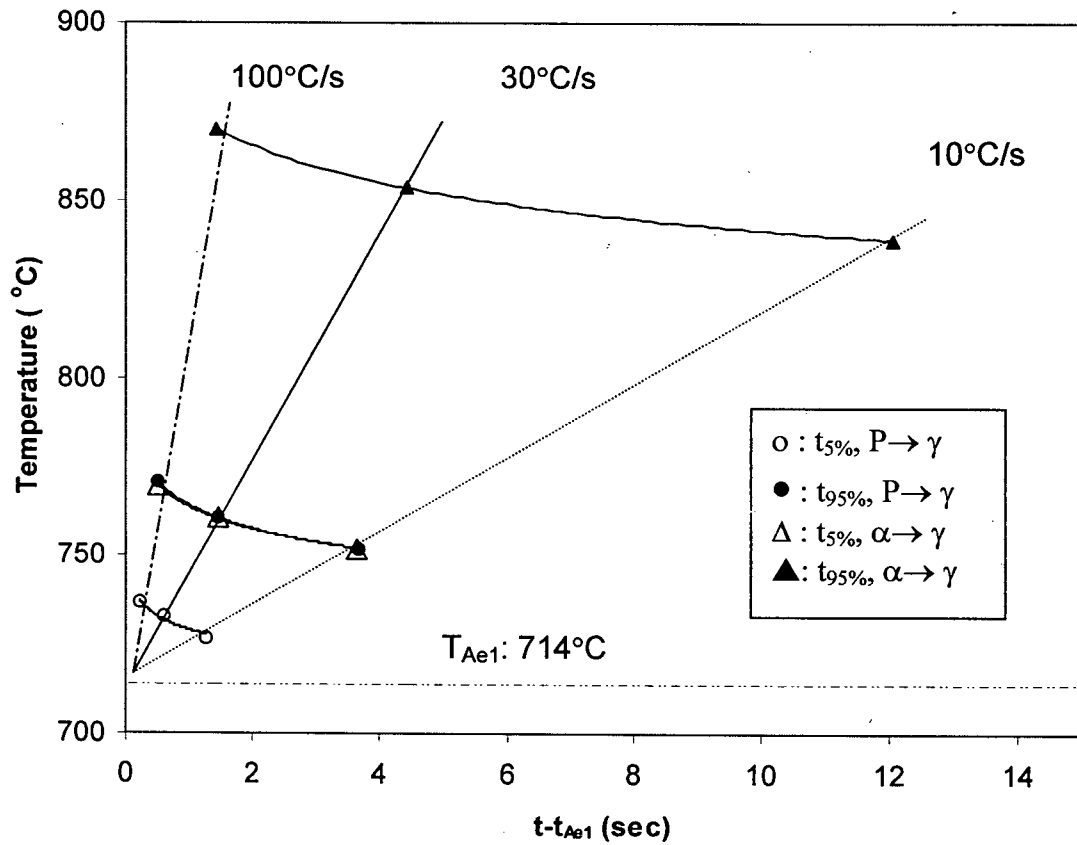
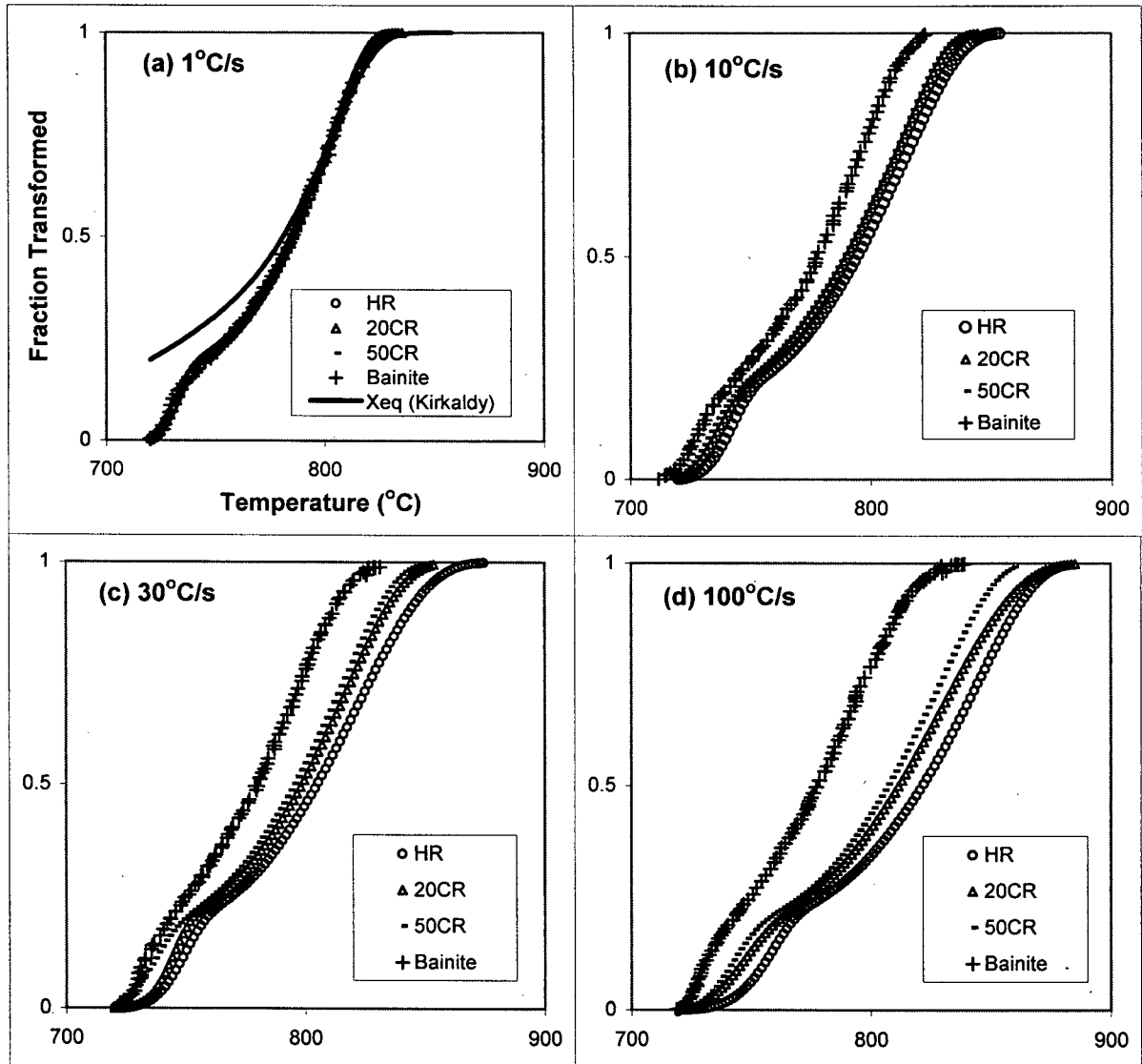


Figure 4-8 : Transformation start and finish times as a function of heating rates for the HR material

#### 4.4 Effect of Initial Microstructure

Figure 4-9 illustrates the effect of initial microstructure on the continuous heating kinetics for selected heating rates. As shown in Figure 4-9 (a), at the heating rate of  $1^{\circ}\text{C/s}$ , all four initial structures reveal the same behavior of austenite formation kinetics. This means that the heating rate of  $1^{\circ}\text{C/s}$  is very close to the equilibrium heating condition, which can be confirmed by comparing these curves to the equilibrium condition,  $X_{eq}$ . In this study, data from Kirkaldy [54] have been taken to calculate equilibrium fractions. Consequently, the transformation from bainite follows the equilibrium condition for all heating rates since it exhibits no heating rate sensitivity, as shown earlier in Figure 4-6.

As the heating rate increases from  $10^{\circ}\text{C/s}$  to  $100^{\circ}\text{C/s}$ , Figure 4-9 (b)~(d), the Bainite material shows much faster transformation than any other materials. Between the HR and CR materials, the transformation rates are in the order of 50CR, 20CR, and HR material. This can be rationalized by a number of reasons. Firstly, the pearlite region might be dispersed and deformed during the cold rolling process resulting in quicker nucleation of austenite. Secondly, the internal free energy accumulated during the cold rolling process can also contribute to easier austenite growth into the ferrite. Finally, there is the possibility that the austenite nucleation occurs not only at pearlite colony boundaries but also at ferrite/ferrite grain boundaries.



**Figure 4-9 : Effect of initial microstructures on continuous heating kinetics with selected heating rates.**

Yang et al. [80] showed that in cold-rolled steels the austenite formed first on the boundaries between deformed and unrecrystallized ferrite grains and then on cementite particles in recrystallized ferrite grains. However, care must be taken in discussing these results since recovery and recrystallization may have taken place to a different degree depending on heating rate before transformation commences in the CR materials. This will be discussed in more detail in section 4.6.

#### **4.5 Microstructural Change During Heating**

Figure 4-10 (a), (b) compares the microstructural changes as a function of temperature in the range of 745 ~ 920°C for a 1°C/s heating rate of the HR and 50CR materials, respectively. These micrographs confirm that the formation of austenite starts from the pearlite region and grows into the ferrite matrix, which is similar to the results documented in the literature [50, 71, 72, 95]. For example, Jacot et al. [95] reported the formation of austenite from ferrite-pearlite microstructure in two steps. The first one is the transformation of pearlite into austenite. Nucleation of austenite grains takes place preferentially at the interfaces between pearlite colonies. The pearlite dissolution is then very fast since the diffusion distances for carbon are relatively short (of the order of the interlamellar spacing).

The second step is the transformation of proeutectoid ferrite into austenite. This transformation is quite sluggish and associated with the partitioning and diffusion of substitutional alloying elements, such as manganese.

It can be also seen that the fraction transformed measured in partly transformed conditions agrees well with the dilatometer measurement, as illustrated in Figure 4-11. However, care must be taken in measuring the volume fraction transformed by metallographic methods, since it is very sensitive to etching conditions of the specimen. For the current measurements a light etching was used so that grain boundaries are not visible. In both HR and 50CR materials, the austenite volume fractions are approximately 20% at 745°C, 45% at 778°C, and 70% at 797°C, respectively.

(a) HR material

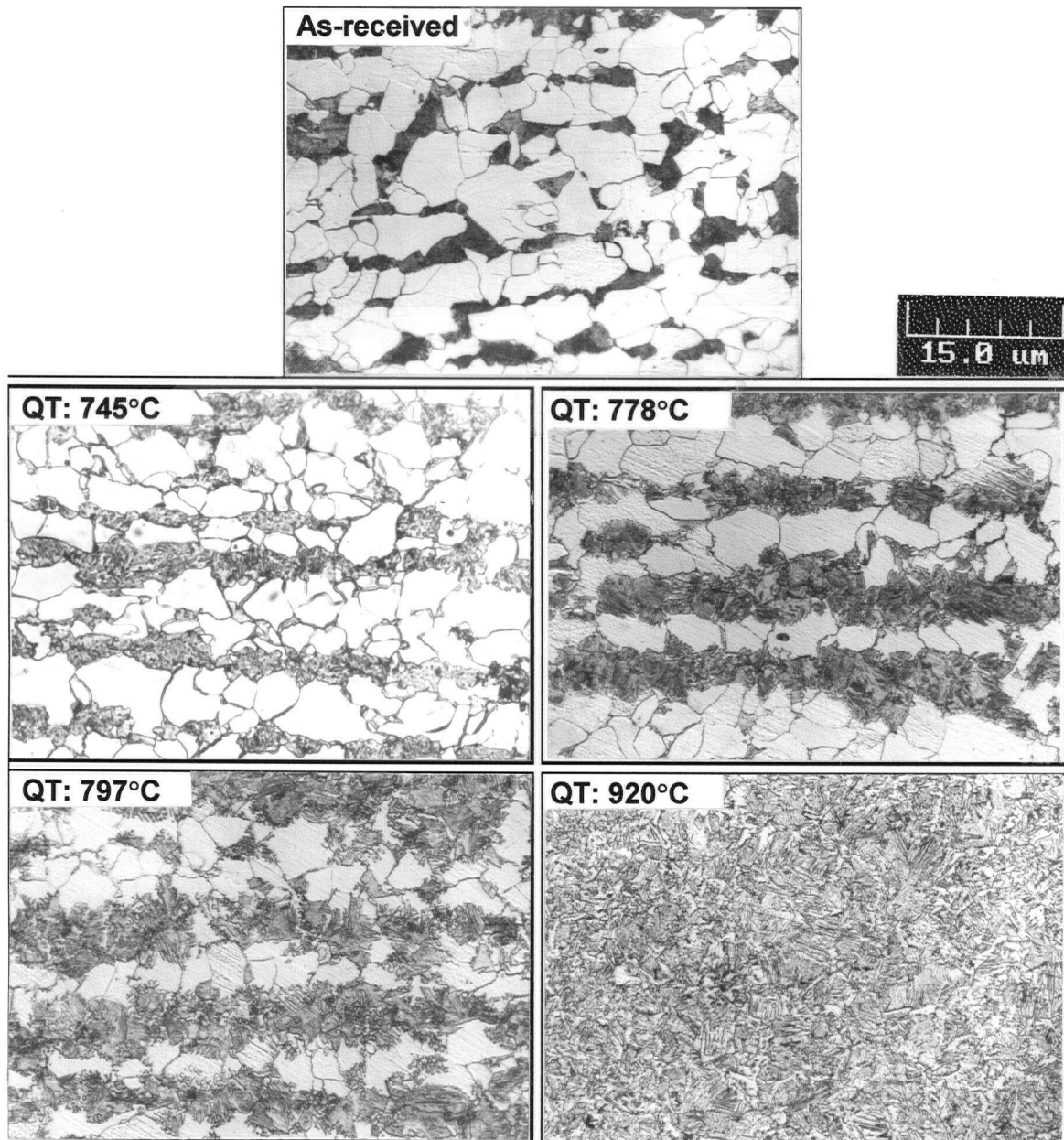
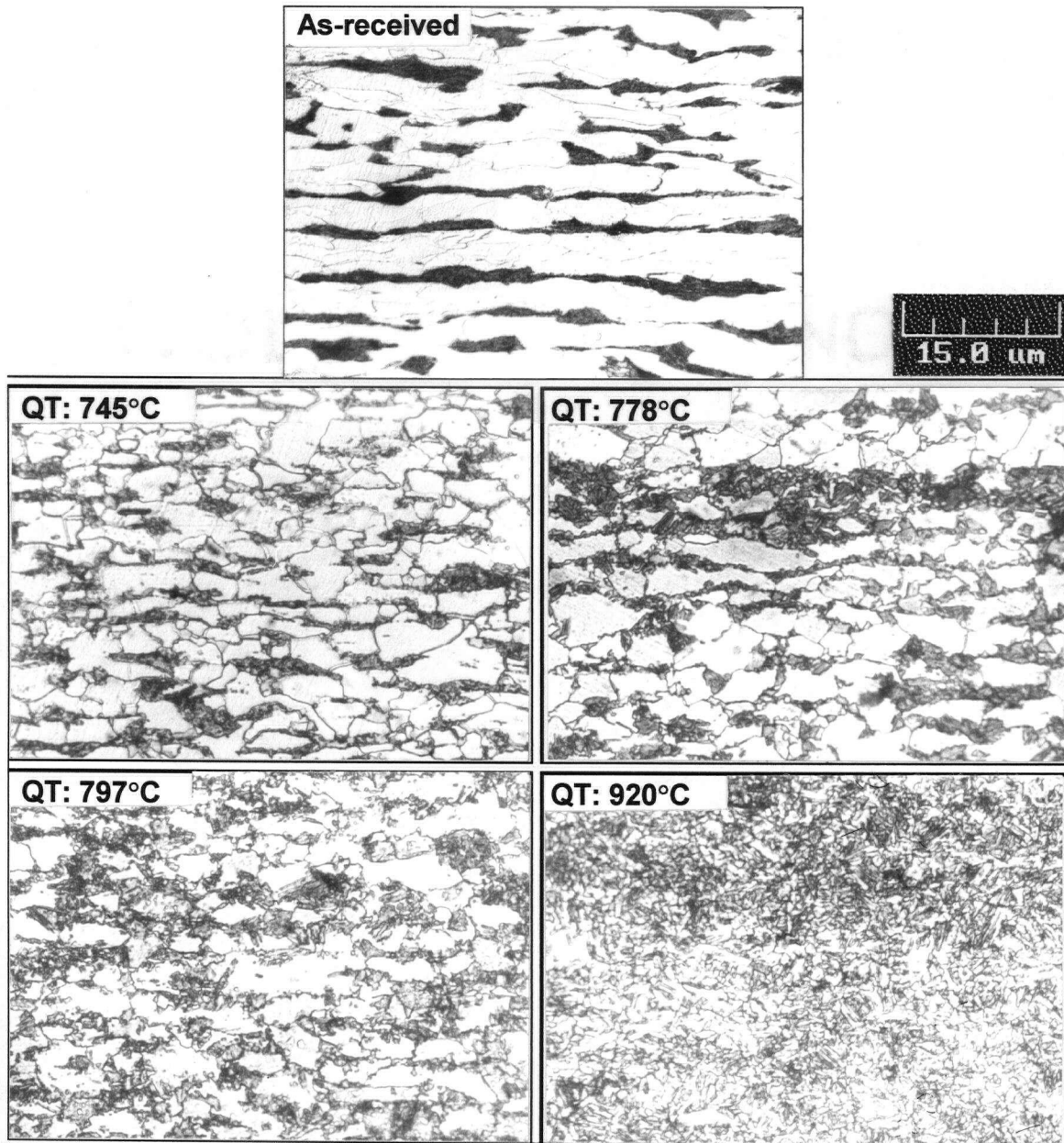
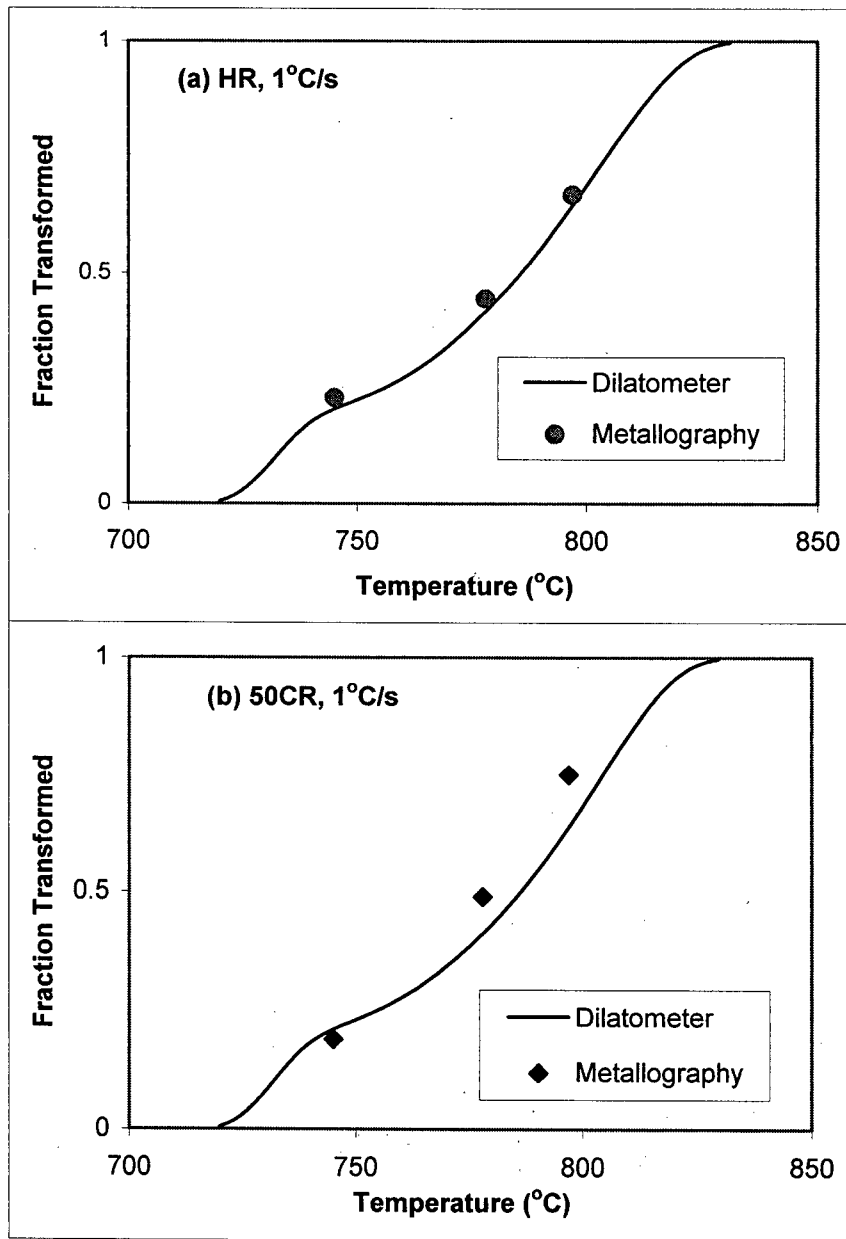


Figure 4-10 : Microstructural changes during continuous heating with a 1°C/s heating rate for various helium quenching temperatures (QT); (a) HR material, (b) 50CR material.

**(b) 50CR material**



**Figure 4-10 : (cont.)**



**Figure 4-11 : Comparison of dilation test results and metallographic examinations for the austenite volume fraction transformed for (a) HR material and (b) 50CR material.**

## 4.6 Effect of Recrystallization

In order to check whether the recrystallization of ferrite happens during heating before transformation, the cold rolled materials were heated at different rates to 745°C. Following helium quenching, the microstructure of the samples were investigated under a light microscope. The temperature of 745°C was chosen since it is the temperature at which the  $P \rightarrow \gamma$  transformation finishes and just before the  $\alpha \rightarrow \gamma$  transformation starts. Figure 4-12 shows the resulting microstructures with different heating rates. In the case of 50CR material, the ferrite grains were fully recrystallized at the 1°C/s heating rate. In the case of the 20CR material, however, it is quite difficult to recognize any changes in the ferrite grain shape.

Further, the micro-hardness of the ferrite grains was measured to confirm the degree of recrystallization for both cold rolled materials. As shown in Figure 4-13, the ferrite hardness decreases steadily with the increase of heating times, which means that the CR materials show an increasing degree of recovery and recrystallization before the  $\alpha \rightarrow \gamma$  transformation as heating rate decreases. Figure 4-14 displays the recrystallization effect on the transformation kinetics. The 50CR materials were first heated to 710°C at 1°C/s during which the matrix ferrite can be recrystallized, and then continuously heated to 950°C at different heating rates of 10, 30, 100°C/s, respectively. After that, the kinetics were

compared with the HR material. As can be seen, the recrystallized 50CR material shows almost the same kinetics as the HR material further confirming that the 50CR material was almost fully recrystallized during heating to 710°C.

The fact that at higher heating rates various degrees of recrystallization are attained before transformation makes an interpretation of the transformation results of the CR materials a complex task. More work is required to quantify the effect of initial CR structure on transformation by separating the phenomena of recovery, recrystallization and transformation. For example, high heating rates can be employed up to 710°C before  $\alpha+P \rightarrow \gamma$  transformation to minimize recovery and recrystallization. This would allow to delineate the actual effect of introducing additional nucleation sites on the austenite formation in CR materials.

(a) 20CR material

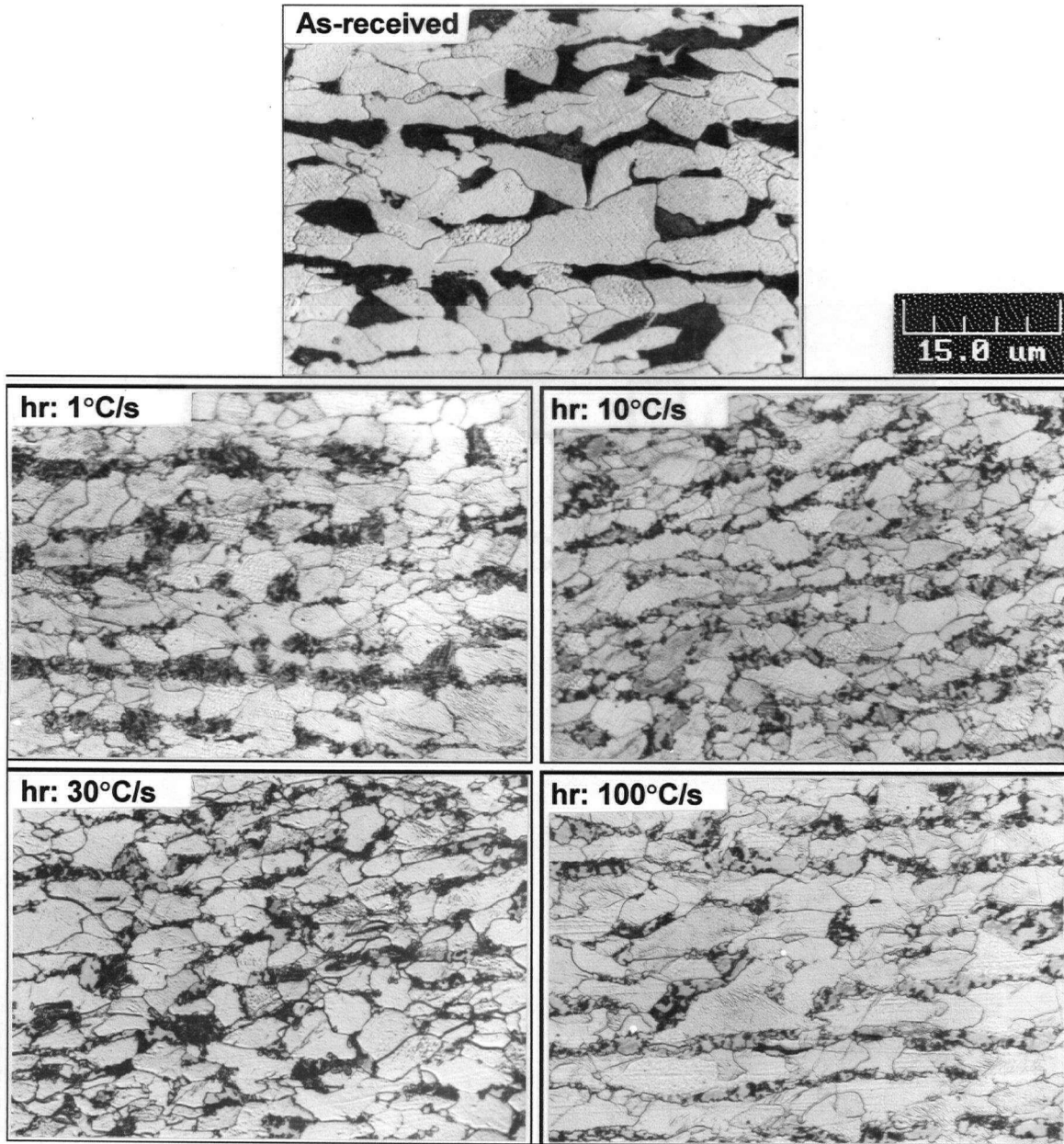
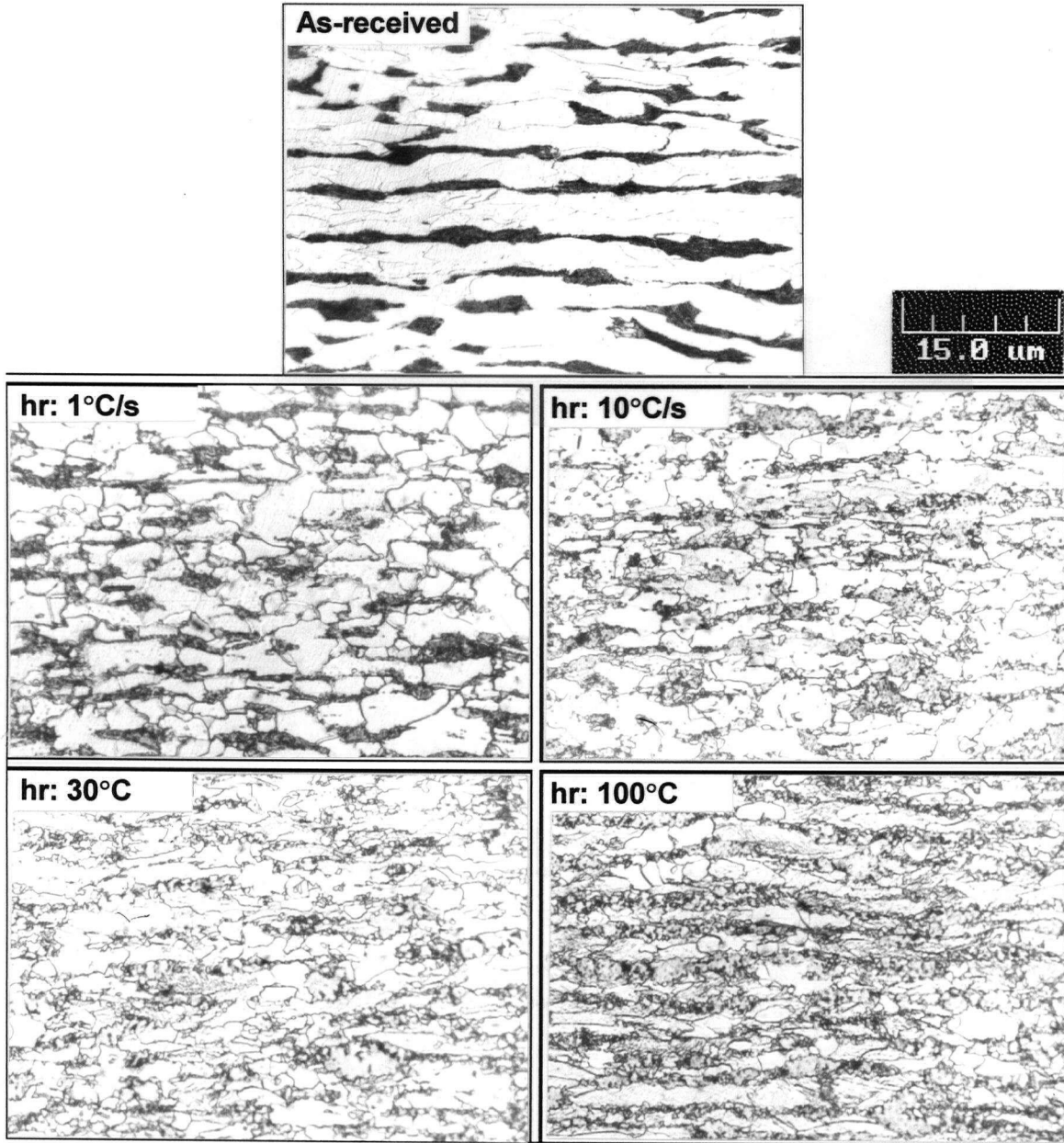
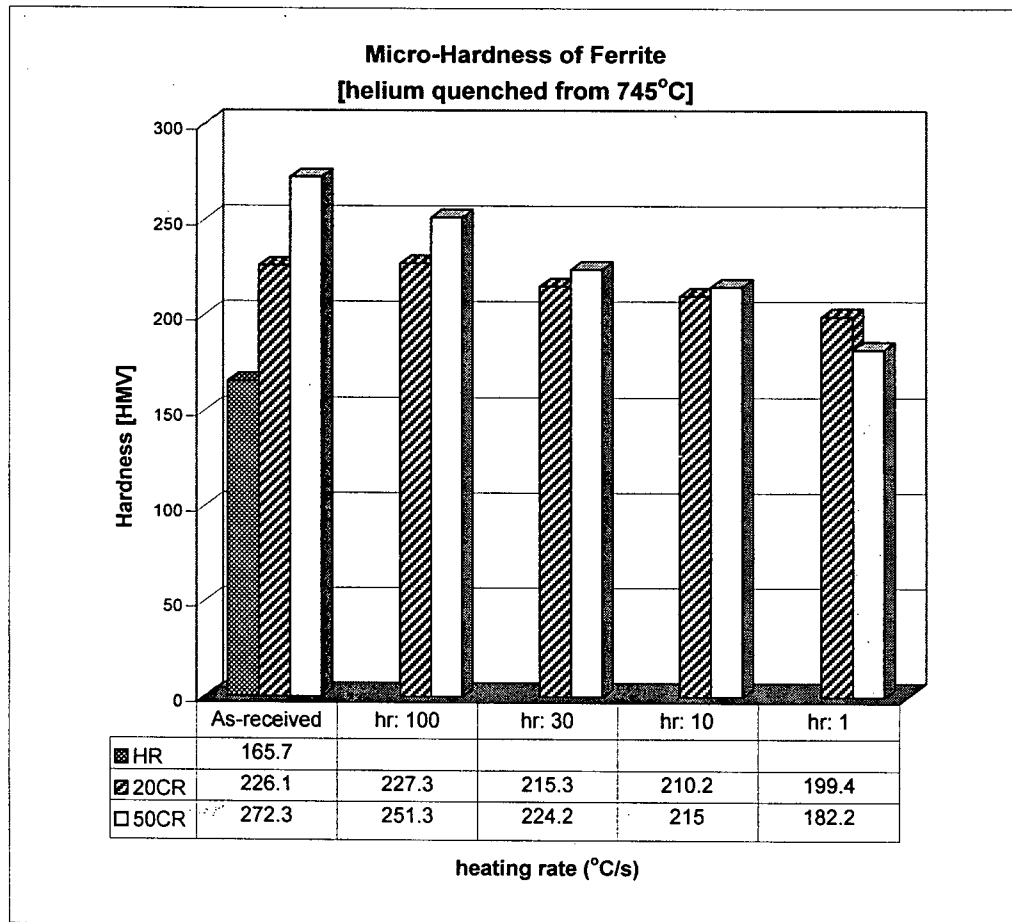


Figure 4-12 : Microstructures helium quenched from 745°C for various heating rates (hr) ; (a) 20CR material, (b) 50CR material.

**(b) 50CR material**



**Figure 4-12 : (cont.)**



**Figure 4-13 : Microhardness changes of ferrite for various heating rates for the CR materials which were helium quenched from 745°C.**

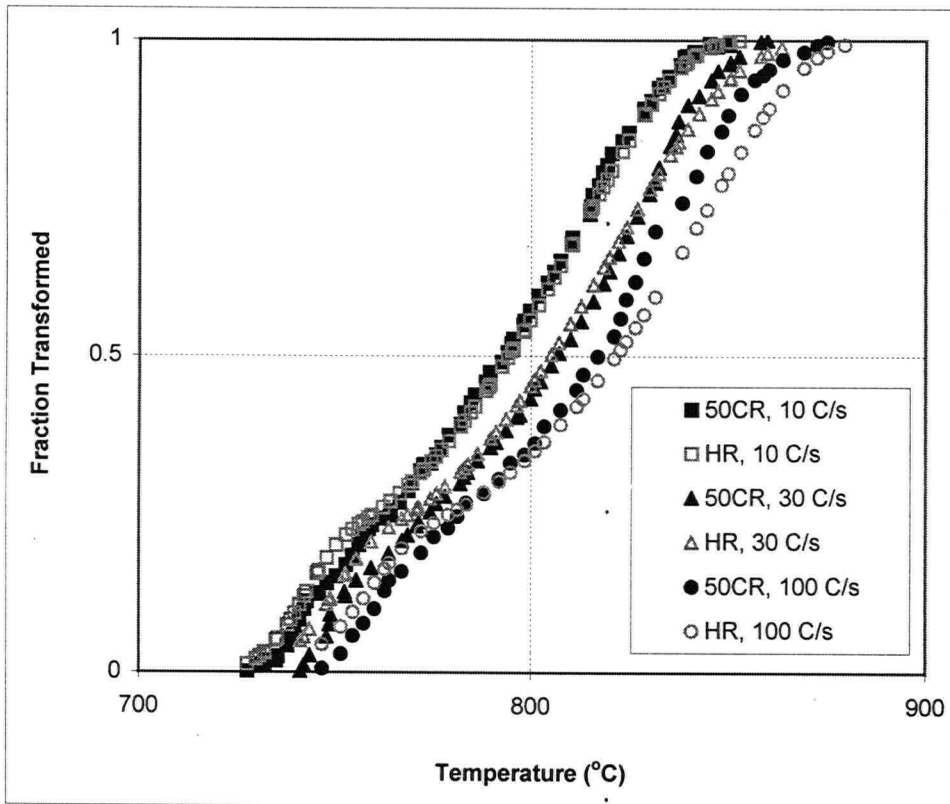


**Figure 4-14 : Comparison of CHT kinetics between the HR and recrystallized 50CR materials for different heating rates.**

## CHAPTER 5 – KINETICS MODELING

### 5.1 Prediction of $A_1$ and $A_3$ Temperatures

The  $A_1$  and  $A_3$  temperatures were estimated following the methods of Andrews [45] and Kirkaldy and Baganis [54]. Based on experimental results, Andrews [45] has reported empirical relationships between chemistry and the approximate  $A_{e3}$ ,  $A_{c1}$ , and  $A_{c3}$  temperatures for different steels, as given by Eq. (2.1), (2.2), and (2.3), respectively.

Kirkaldy and Baganis [54] formulated the  $A_{e1}$  and  $A_{e3}$  temperatures based on the thermodynamics of the ternary Fe-C-X system for a wide range of alloying elements, including Fe-C-Mn plain-carbon steels. The approach is presented in detail in [54].

The results of this analysis are compared in Table 5.1 with the values determined from the Andrews equation. There is good agreement between both methods. In this paper, the Kirkaldy and Baganis method was used in subsequent analysis since this method employs basic thermodynamic data.

**Table 5.1:  $A_1$  and  $A_3$  temperatures ( $^{\circ}\text{C}$ ) calculated for 0.16C-1.38Mn-0.24Si steel using methods developed by Andrews [45] and Kirkaldy and Baganis [54].**

Source	Temperature	Estimated Value ( $^{\circ}\text{C}$ )
Andrews [45]	Ac1	714
	Ac3	828
	Ae3	817
Kirkaldy [54]	Ae1	714
	Ae3	820

## **5.2 Modeling of Continuous Heating Kinetics**

### ***5.2.1 Application of the Additivity Rule***

The method used in this paper for calculating phase transformations during continuous heating is based on the additivity rule. The additivity principle has been used by several authors [11-13] to describe the phase transformation kinetics during austenitization of steels and it can be briefly described as follows. The principle of this method involves dividing the continuous heating transformation curve into a series of small time segments. The fraction

of new phase formed is then calculated by assuming additive isothermal conditions for each time segment.

In this study, the  $P+\alpha \rightarrow \gamma$  transformation was considered a combination of two individual reactions of  $P \rightarrow \gamma$  and  $\alpha \rightarrow \gamma$ . This means that those two transformations were dealt with separately. The transformation kinetics of both reactions can be described with Avrami equations, one for the dissolution of pearlite and the other for the transformation of ferrite.

$$X_P = 1 - \exp[-b_P t^{n_P}] \quad (5.1)$$

$$X_F = 1 - \exp[-b_F t^{n_F}] \quad (5.2)$$

In order to apply the Avrami equation to account for continuous heating conditions it must be modified in the differential form, i.e.,  $\frac{dX}{dt} = nb^{1/n} [-\ln(1-X)]^{\frac{n-1}{n}} (1-X)$  (refer to Eq. 2.13). If  $n$  is a constant and only  $b$  depends on the transformation temperature, the additivity rule can be applied.

The procedure to determine  $n$  and  $b$  values for each transformation is the same and the following three steps were used.

- (1) converting true fraction into normalized fraction
- (2) selecting  $n$  value
- (3) calculating  $b$  value as a function of temperature

The fraction transformed in the Avrami equation,  $X$ , is a normalized fraction. Hence the calculated fraction from the dilatometer, which is the true fraction, must be converted into a normalized term by

$$X_N = \frac{X_T}{X_{eq}} \quad (5.3)$$

where  $X_N$ ,  $X_T$ , and  $X_{eq}$  are the normalized, true, and equilibrium fraction, respectively.

Selecting an  $n$ -value, the value of  $b$  can be calculated from the experimental data by rearranging the rate equation (2.13); i.e.,

$$b = \left\{ \frac{dX/dt}{n(1-X)[- \ln(1-X)]^{n-1/n}} \right\}^n \quad (5.4)$$

This procedure is performed for a given test series with different heating rates. The selected  $n$ -value is varied such that  $b$  becomes independent of heating rate. At this specific  $n$  value,

$b$  can be fitted as a function of temperature. For this work, it is convenient to plot  $\ln b$  vs. temperature and obtain the function  $b$  from a least-squares fit. As an example, this plot is shown in Figure 5-1(a) and (b) for the  $P \rightarrow \gamma$  and  $\alpha \rightarrow \gamma$  transformation, respectively, of the HR material.

The kinetic parameters for the HR, 20CR, and 50CR materials are summarized in Table 5.2. In this study, the best fit of  $\ln b$  as a function of temperature is fulfilled when  $n=0.9$  is taken for the  $P \rightarrow \gamma$  transformation and  $n=0.7$  for the  $\alpha \rightarrow \gamma$  part.

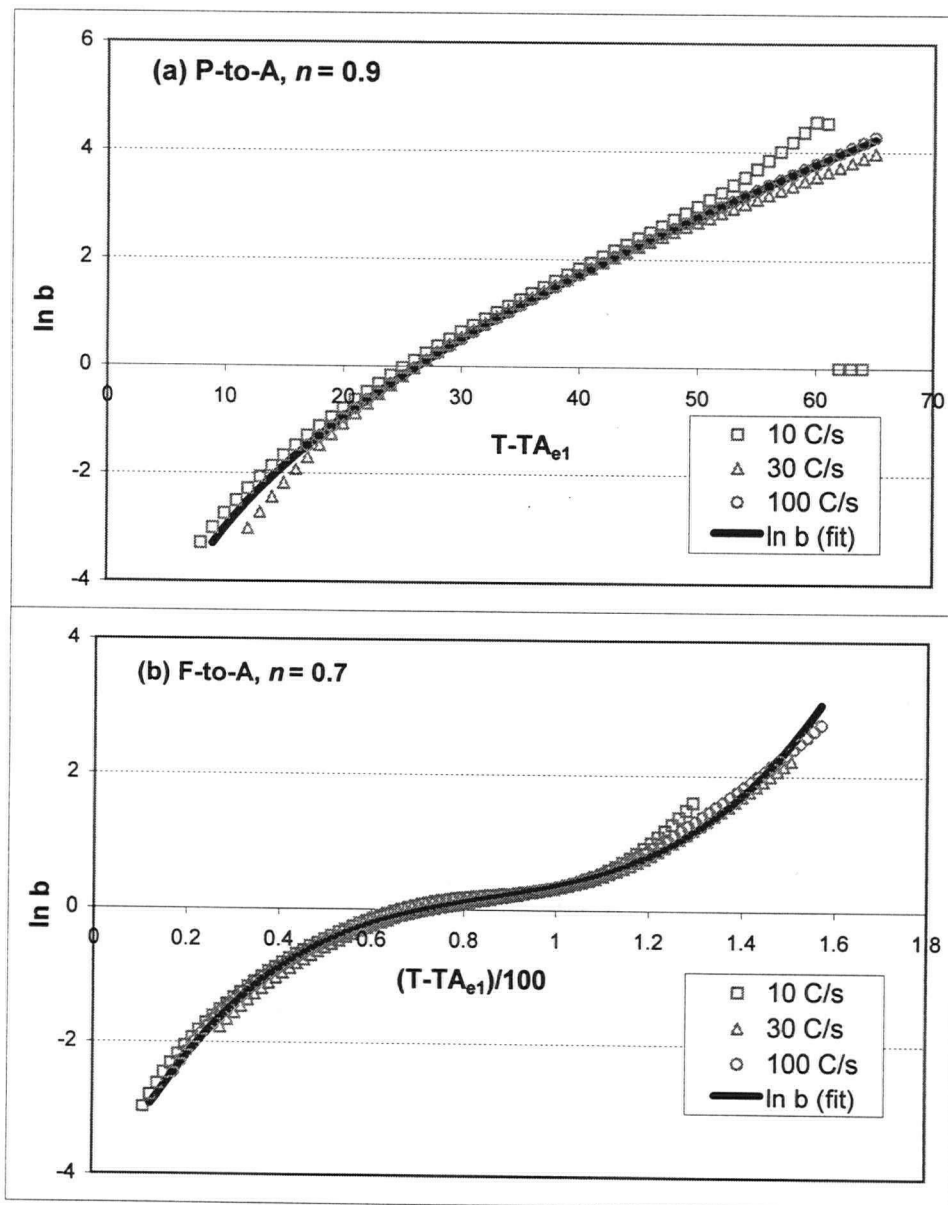


Figure 5-1 : Fitted  $\ln b$  values as a function of transformation temperatures for (a) P $\rightarrow$  $\gamma$  and (b)  $\alpha \rightarrow \gamma$  transformation of the HR material.

**Table 5.2 : Calculated kinetic parameters for modeling the continuous heating transformations of the HR, 20CR, and 50CR materials.**

Materials		HR		20CR		50CR	
		P → γ	α → γ	P → γ	α → γ	P → γ	α → γ
ln b fitting parameters	a	-8.489	5.789	-9.778	5.152	-6.775	7.524
	b	0.060	-14.929	0.063	-13.622	0.048	-18.440
	c	2.118	13.960	2.699	13.262	2.042	16.121
	d	-	-4.459	-	-3.940	-	-4.114
Remarks		<p>(1) ln b vs. temperature :</p> <p>for P → γ : <math>Y_1 = a + bx + c \ln x</math>, where <math>Y_1 = \ln b_p</math>, <math>x = T - T_{Ae1}</math></p> <p>for α → γ : <math>Y_2 = ax^3 + bx^2 + cx + d</math>, where <math>Y_2 = \ln b_F</math>, <math>x = (T - T_{Ae1})/100</math></p> <p>(2) n values: 0.9 (P → γ), 0.7 (α → γ)</p>					

### 5.2.2 Comparison of model and experimental data

From the calculated kinetic parameters, shown in Table 5.2, the  $P+\alpha \rightarrow \gamma$  transformation can be calculated using models that are a combination of  $P \rightarrow \gamma$  and  $\alpha \rightarrow \gamma$  reactions. If the  $P \rightarrow \gamma$  transformation is considered first, the calculation of fraction of austenite formed is initiated at the transformation start time,  $t_{AV_{CHT,P}}$ , and uses the parameters  $n_P$  and  $\ln b_P(T)$ , as shown in Figure 5-2. In the first time segment, which has an average temperature  $T_1$ , the fraction of austenite formed (normalized to  $X_{A,N1}$ ) is calculated from:

$$X_{A,N1} = 1 - \exp[-b_P(T_1)t_1^{n_P}] \quad (5.5)$$

where  $t_1$  is the first time increment,  $\Delta t$ , after  $t_{AV_{CHT,P}}$ . This value of fraction of austenite formed is then corrected to the true fraction of austenite formed by

$$X_{A,T1} = X_{eq}(T_1)X_{A,N1} \quad (5.6)$$

where  $X_{eq}$  is the equilibrium volume fraction, which is equivalent to the pearlite volume fraction of the initial microstructure, i.e., 18% (=0.18) for this study.

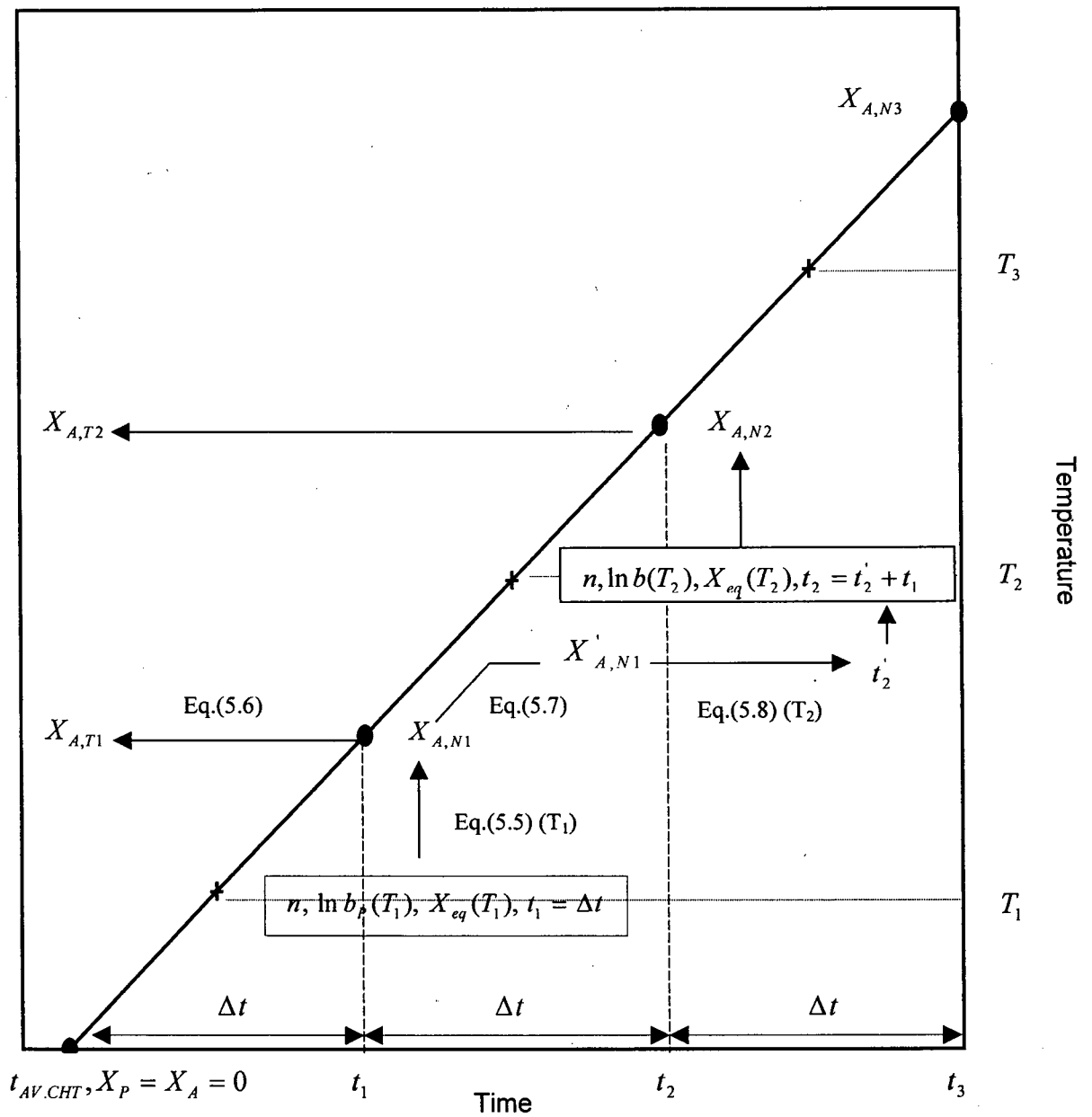


Figure 5-2 : Schematic diagram showing the calculation procedure to predict continuous heating kinetics for the P→ $\gamma$  transformation by assuming additive isothermal conditions.

In the second heating segment, since each isothermal temperature would produce a different fraction of austenite, it is first necessary to change  $X_{A,N1}$  to its equivalent fraction at  $T_2$ . This can be calculated from:

$$X_{A,N1}' = \frac{X_{eq}(T_1)}{X_{eq}(T_2)} X_{A,N1} \quad (5.7)$$

Therefore the time,  $t_2$ , required to produce  $X_{A,N1}'$  at the temperature  $T_2$  is calculated using the parameters  $n_P$  and  $\ln b_P(T_2)$ , such that:

$$t_2' = \left[ \frac{-\ln(1 - X_{P,N1}')}{b_P} \right]^{1/n_P} \quad (5.8)$$

The time segment,  $\Delta t$ , is added to this calculated value and a new fraction of ferrite transformed,  $X_{A,N2}$ , is calculated.  $X_{A,N2}$  is converted to the true fraction of austenite formed using the  $T_2$  equivalent of Eq. (5.6). This procedure is repeated until the pearlite-to-austenite transformation is completed.

The same procedure is followed to predict the  $\alpha \rightarrow \gamma$  transformation kinetics. Using Eq. (5.5), the parameters  $b_F$  and  $t_1^{n_F}$  are substituted which correspond to the  $\alpha \rightarrow \gamma$  transformation.

In this case, however,  $X_{eq}$  is the equilibrium volume fraction determined by the Fe-C phase diagram based on the Kirkaldy and Baganis data [54]. Compared with the previous P→ $\gamma$  transformation, this is the only difference and the rest of the procedure is the same.

The predicted kinetics of the pearlite-ferrite to austenite transformation is compared to the experimental kinetics for the HR, 20CR, and 50CR materials in Figure 5-3, 5-4, and 5-5, respectively. The results for the high heating rates where kinetic effects are relevant exhibit excellent agreement for all three initial ferrite-pearlite structures. However, it must be noted that the model is a complete empirical approach. The determined  $n$ -values do not follow the classical cases of Table 2.1. For a better understanding of the transformation mechanisms, more fundamentally based models need to be developed. This is difficult to do from only CHT data. Additional isothermal data would provide a better base for any modeling approach.

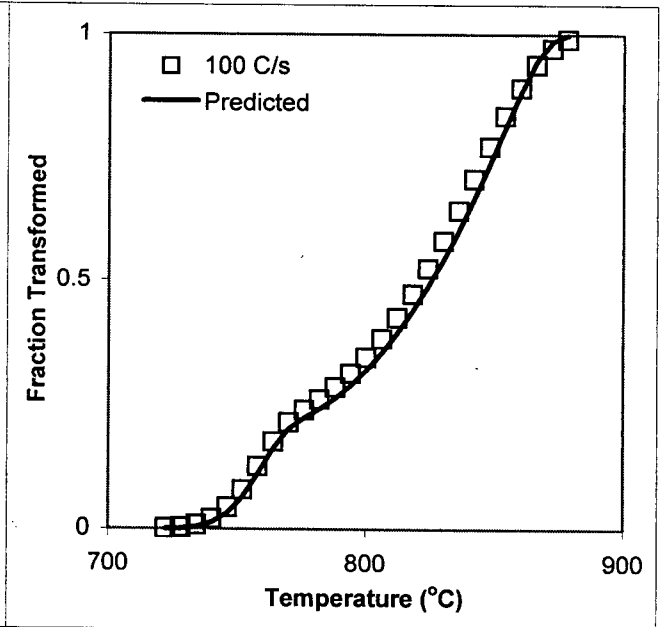
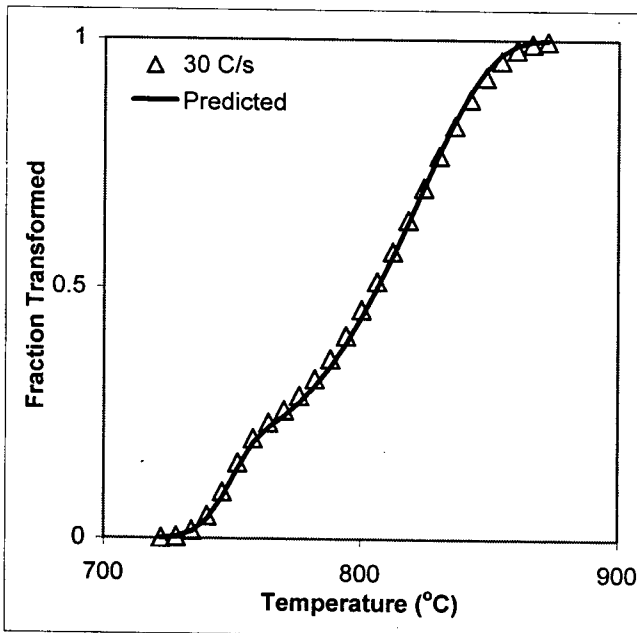
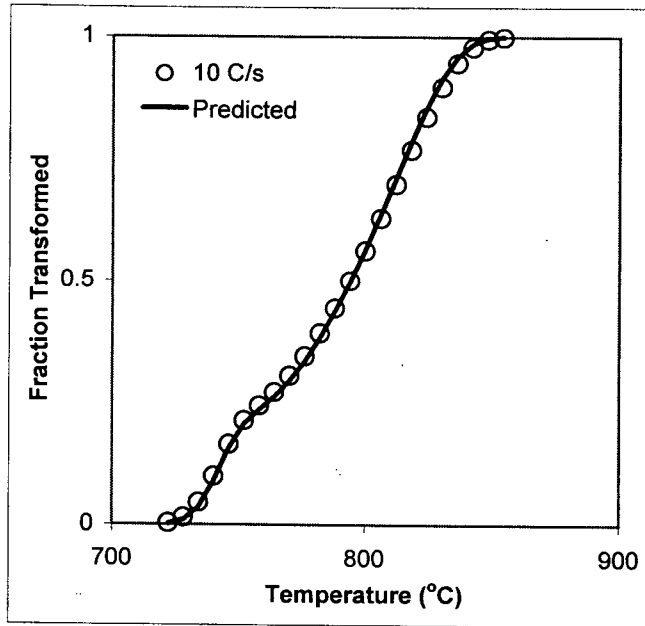


**Figure 5-3 : Comparison between experimental data and predicted continuous heating kinetics for the HR material.**

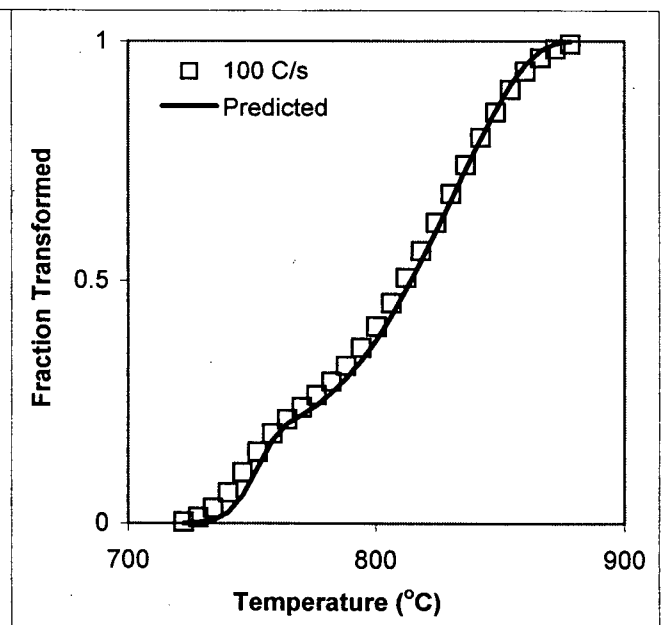
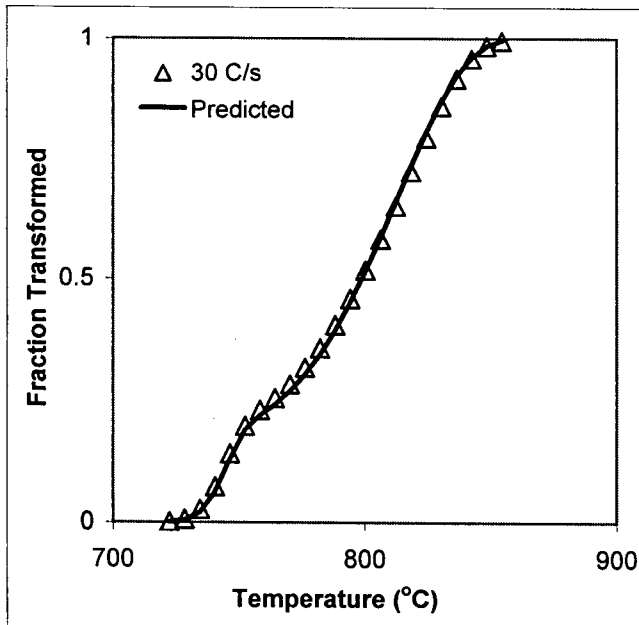
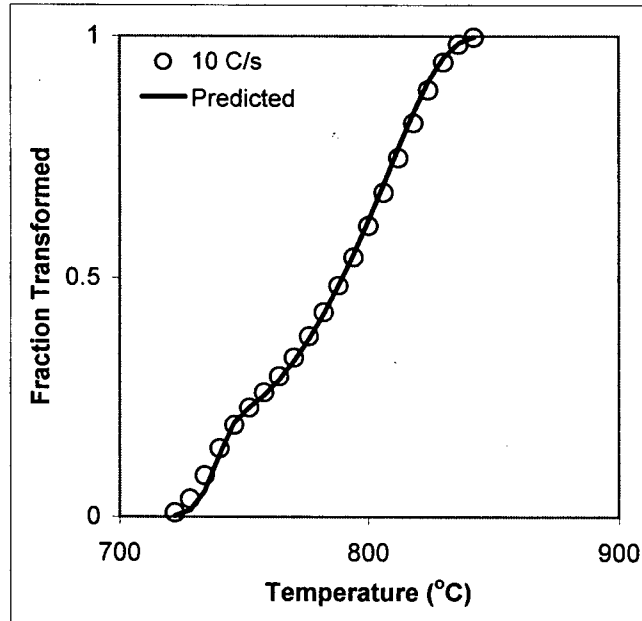


**Figure 5-4 : Comparison between experimental data and predicted continuous heating kinetics for the 20CR material.**

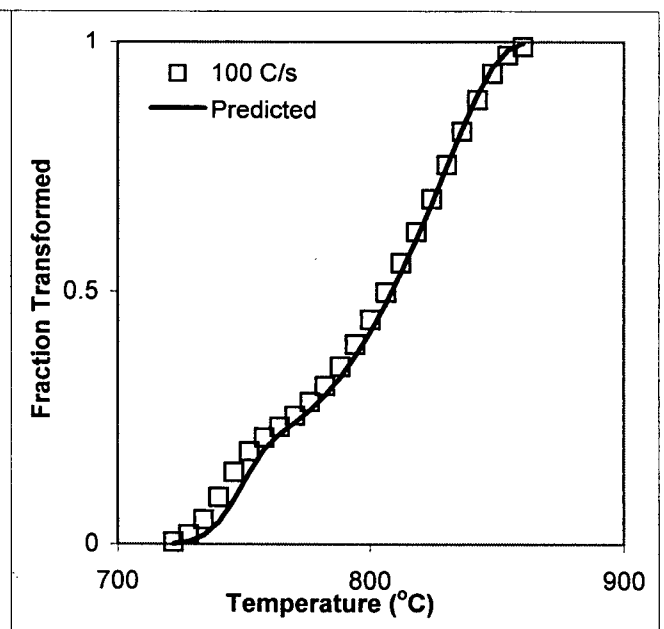
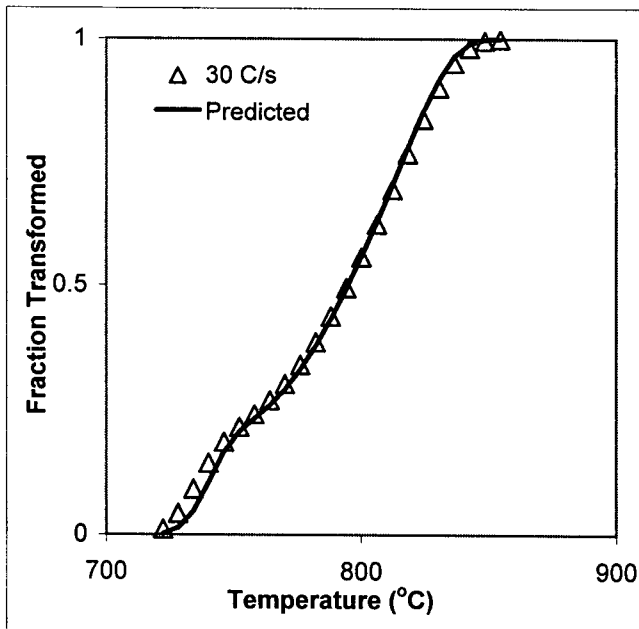
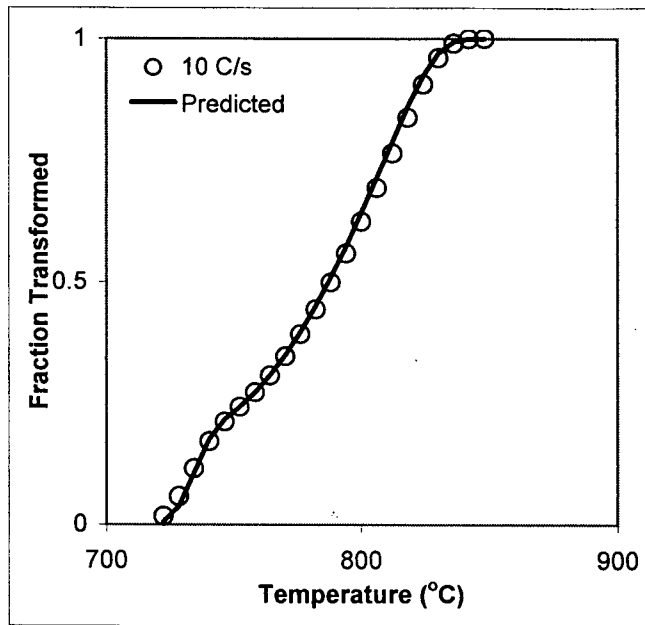


**Figure 5-5 : Comparison between experimental data and predicted continuous heating kinetics for the 50CR material.**

## CHAPTER 6 – CONCLUSIONS AND FUTURE WORK

### 6.1 Conclusions

The following conclusions summarize the results and discussion of the present studying the kinetics of austenite formation from pearlite-ferrite structure in a multi-phase steel.

- (1) In good agreement with published results, the pearlite-ferrite to austenite transformation can be characterized by two substages. The first involves the transformation of pearlitic regions to austenite, while the second consists of the consumption of ferrite matrix by the austenite phase. These two substages are not necessarily completely distinct from each other in time; in fact, the  $\alpha \rightarrow \gamma$  transformation starts just before the completion of the pearlite dissolution, resulting in a short interval of overlap between those two stages. Presumably, the transformation in pearlite occurs more quickly because the carbide lamellae provide a ready source of carbon, reducing the diffusion distance in the  $\gamma$  phase.
- (2) As heating rate increases the transformation start and finish temperature,  $T_S$  and  $T_F$ , increase. The CHT kinetics of the CR material are less sensitive to the heating rates than the HR material. Among different initial structures, the Bainite material reveals the fastest transformation rates followed by the 50CR, 20CR, and HR materials,

respectively. This trend is consistent with austenite formation starting from the dissolved pearlite region and then the austenite grows into the ferrite matrix. As a result, the Bainite material, which consists of a fine mixture of  $\alpha$  and  $\text{Fe}_3\text{C}$ , can supply abundant austenite nucleation sites and short diffusion distance, resulting a transformation which follows equilibrium even for heating rates as high as  $100^\circ\text{C/s}$ . Cold rolling elongates ferrite grains and fragments pearlite lamellae, thus increasing the nucleation sites of austenite and thereby showing faster transformation than the HR material.

- (3) A mathematical model based on the Avrami equation and the additivity principle has been successfully used to reproduce the kinetics of the  $\text{P}+\alpha \rightarrow \gamma$  transformation during continuous heating. By adopting a curve-fitting technique, the total  $\text{P}+\alpha \rightarrow \gamma$  transformation could be handled by a combination of two separate reactions, i.e.,  $\text{P} \rightarrow \gamma$  and  $\alpha \rightarrow \gamma$ . Then, the transformation kinetics were characterized in terms of the Avrami parameters  $n$  and  $b$ . Average values of  $n = 0.9$  and  $0.7$  were supposed for the  $\text{P} \rightarrow \gamma$  and  $\alpha \rightarrow \gamma$  transformation, respectively. The results for the HR and CR materials revealed good agreement between experimental data and predictions.

## 6.2 Comments on Future Work

The materials used in the present work contained some banded regions which could affect the phase transformation kinetics. This may be one major reason why the results of the dilation tests revealed variations. In order to prepare specimens with little banded structure, a preliminary heat treatment such as austenitization and isothermal transformation suggested in [71] is recommended. Considering the effect of cold rolling on transformations, more work is required to separate the phenomena of recovery and recrystallization from phase transformations. One approach to the problem would be to apply rapid heating up to 710°C, just below the transformation start temperature, followed by selected heating rates to investigate the transformation process. For a better understanding of the transformation mechanisms, it is planned to implement the influence of the intercritical annealing conditions, i.e., isothermal tests. This would enhance the accuracy of the proposed model, since the isothermal data would be specific to the material conditions.

## REFERENCES

- 1 R.A. Heimbuch: *40th MWSP CONF. PROC., ISS*, (1998), p.3
- 2 T. Heller, B. Engl, B. Ehrhardt and J. Esdohr: *40th MWSP CONF. PROC., ISS*, (1998), p.25
- 3 K. Eberle, Ph. Harlet, P. Cantinieaux and M. Vande Populière: *40th MWSP CONF. PROC., ISS*, (1998), p.251
- 4 G.A. Roberts, R.F. Mehl: *Trans. ASM*, **31**, (1943), p.613
- 5 G. Molinder: *Acta Metall.*, **4**, (1956), p.565
- 6 G.R. Speich, A. Szirmae: *Trans. TMS AIME*, **245**, (1968), p.1063.
- 7 R.R. Judd and H.W. Paxtom: *Trans. TMS-AIME*, **242**, (1968), p.206
- 8 M. Hillert, K. Nilsson, and L.E. Torndahl: *J. Iron and Steel Inst.*, (1971), p.49
- 9 C. Atkinson, T. Akbay, and R.C. Reed: *Acta metall. mater.*, **43**, (1995), p.2013
- 10 T. Akbay, R.C. Reed, and C. Atkinson: *Acta metall. mater.*, **47**, (1994), p.1469
- 11 J.B. Leblond and J. Devaux: *Acta metall.*, **32**, (1984), p.137
- 12 S. Denis, D. Farias, and A. Simon: *ISIJ Int.*, **32**, (1992), p.316
- 13 T.T. Pham, E.B. Hawbolt, and J.K. Brimacombe: *Met. Trans.*, **26A**, (1995), p.1987
- 14 M. Umemoto: *The 131st-132nd Nishiyama Memorial Seminar*, ISIJ, Tokyo, (1989), p.97
- 15 M. Suehiro, K. Sato, Y. Tsukano, H. Yada, T. Senuma and Y. Matsumura: *Trans.*

- ISIJ*, **27**, (1987), p.439
- 16 Y. Saito: *The 131st-132nd Nishiyama Memorial Seminar*, ISIJ, Tokyo, (1989), p.185
  - 17 T. Matsuoka and K. Yamamori: *Metall. Trans.*, **6A**, (1975), p.1613
  - 18 A.K. Sinha: *Ferrous Physical metallurgy*, Butterworths, Stoneham, (1989), p.235
  - 19 J.W. Morrow, G. Tither and R. M. Buck: *in Formable HSLA and Dual-Phase Steels*, Davenport A. T., ed., AIME, Warrendale, PA, (1979), p.152
  - 20 P.R. Mould and C. C. Skena: *in Formable HSLA and Dual Phase Steels*, Davenport A. T., ed., AIME, Warrendale, PA, (1979), p.181
  - 21 N. Matsumura and M. Tokizane: *ISIJ*, **70**, (1984), p.96
  - 22 D.A. Korzekwa, D.K. Matlock and G. Krauss: *Metall. Trans. A.*, **15A**, (1984), p.1221
  - 23 T. Furukawa and M. Tanino: *in Fundamentals of Dual-Phase Steels*, Kot R. A. and Bramfitt B. L., eds., AIME, New York, (1981), p.221
  - 24 H.Q. Liu, C. Zhu and G. C. Li: *Theoretical and Applied Fracture Mechanics*, **19**, (1993), p.127
  - 25 S. Sekino and N. Mori: *Proc. Int. Conf. Sci. Technol. Iron Steel*, Tokyo, (1971), p.1181
  - 26 H.T. Zhang, C. F. Huang, H. J. Chen and G. Y. Pang: *International Symposium on Low-Carbon Steels for the 90's*, R. Asfahani and G. Tither ed., TMS, (1993), p.367
  - 27 R.P. Krupitzer: *in Fundamentals of Dual-Phase Steels*, R. A. Kot and B. L. Bramfitt eds., AIME, New York, (1981), p.315
  - 28 K. Sugimoto, T. Sakaki, T. Fukusato and O. Miyagawa: *ISIJ*, **71**, (1985), p.70

- 29 R.L. Reuben and T. N. Baker: *Mater. Sci. and Eng.*, **63**, (1984), p.229
- 30 Z.H. Jiang, Z. Z. Guan and J. S. Lian: *Mater. Sci. Eng. A*, **190**, (1995), p.55
- 31 L.X. Hua and S. Z. Cheng: *Proceedings of the 5th International Congress of Heat Treatment of Materials*, Budapest, (1986), p.483
- 32 N. Nagao and K. Kunishige: *Accelerated Cooling of Steel*, (1985), p.463
- 33 M. Sarwar and R. J. Priestner: *J. of Mater. Sci.*, **31**, (1996), p.2091
- 34 P.H. Chang and A. G. Preban: *Acta Metall.*, **33**, (1985), p.897
- 35 H.C. Chen and G. H. Cheng: *J. of Mater. Sci.*, **24**, (1989), p.1991
- 36 K. Sugimoto, M. Kobayashi, and S. Hashimoto: *Metall. Trans. A*, **23A**, (1992), p.3085
- 37 Y. Sakuma, O. Matsumura, and H. Takechi: *Metall. Trans. A*, **22A**, (1991), p.489
- 38 K. Sugimoto, N. Usui, M. Kobayashi, and S. Hashimoto: *ISIJ Inter.*, **32**, (1992), p.1311
- 39 W.C. Jeong, D. K. Matlock and G. Krauss: *Mater. Sci. Eng. A*, **165**, (1993), p.1
- 40 K. Sugimoto, M. Misu, M. Kobayashi, and H. Shirasawa: *ISIJ Inter.*, **33**, (1993), p.775
- 41 P. Jacques, K. Eberle, Ph. Harlet, and F. Delannay: *40th MWSP CONF. PROC.*, ISS, (1998), p.239
- 42 J.B. Gilmour, G.R. Purdy, and J.S.Kirkaldy: *Metall. Trans.*, **3**, (1972), p.1455
- 43 J.B. Gilmour, G. R. Purdy and J. S. Kirkaldy: *Metall. Trans.*, **3**, (1972), p.3213
- 44 A. Jacot and M. Rappaz: *Acta mater.*, **45**, (1997), p.575

- 45 K.W. Andrews: *J. Iron Steel Inst.*, (1965), p.721
- 46 R.W.K. Honeycombe and H. K. D. H. Bhadeshia: *Steels Microstructure and Properties*, 2nd edition, Edward Arnold, London, (1995), p.60
- 47 J.A. Jones: *J. Iron Steel Inst.*, **107**, (1923), p.439
- 48 I. Tsukatani, S. Hashimoto and T. Inoue: *ISIJ Int.*, **31**, (1991), p.992
- 49 H.K.D.H. Bhadeshia: *Bainite in Steels*, The Institute of Materials, London, (1992), p.72
- 50 M.M. Souza, J.R.C. Guimaraes, and K.K. Chawla: *Met. Trans. A*, **13A**, (1982), p.575
- 51 C. Fossaert, G. Rees, T. Maurickx and H. K. D. H. Bhadeshia: *Metall. Trans.*, **26A**, (1995), p.21.
- 52 R.A. Farrar and Z. Zhang: *J. of Mater. Sci. Letters*, (1993), p.1606.
- 53 C. García de Andrés, F. G. Caballero, C. Capdevila and H. K. D. H. Bhadeshia: *Scripta Materialia*, **39**, (1998), p.791
- 54 J.S. Kirkaldy and E.A. Baganis: *Met. Trans. A*, **9A**, (1978), p.495
- 55 R.W.K. Honeycombe and H. K. D. H. Bhadeshia: *Steels Microstructure and Properties*, 2nd edition, Edward Arnold, London, (1995), p.68
- 56 R.W.K. Honeycombe and H. K. D. H. Bhadeshia: *Steels Microstructure and Properties*, 2nd edition, Edward Arnold, London, (1995), p.133
- 57 V.F. Zackay, E.R. Parker, D. Fahr, and R. Bush: *Trans. ASM*, **60**, (1967), p.252
- 58 K. Sugimoto, M. Kobayashi, and S. Hashimoto: *J. JIM*, **54**, (1990), p.657
- 59 K. Sugimoto, M. Kobayashi, S.I. Yasuki and S.I. Hashimoto: *Mater. Trans., JIM*, **36**,

- (1995), p.632
- 60 Ed. by G.B. Olson and W.S. Owen: *Martensite*, ASM Inter., (1992), p.228
- 61 M. Cohen: *Trans. ASM*, **41**, (1949), p.35
- 62 H. Onodera and I. Tamura: *Proc. U.S.-Japan seminar on mechanical behavior of metals and alloys associated with displacive transformation*, Troy, NY, (1979), p.24
- 63 G.B. Olson and M. Cohen: *Proc. U.S.-Japan seminar on mechanical behavior of metals and alloys associated with displacive transformation*, Troy, NY, (1979), p.7
- 64 P.C. Maxwell, A. Goldberg, and J.C. Shyne: *Met. Trans.*, **5**, (1974), p.1305
- 65 T. Minote, S. Torizuka, A. Ogawa and M. Niikura: *ISIJ Int.*, **36**, (1996), p.201
- 66 T. Akbay and C. Atkinson: *J. of Mat. Sci.*, **31**, (1996), p.2221
- 67 H.K.D.H. Bhadeshia and D.V. Edmonds: *Metall. Trans. A*, **10A**, (1979), p.895
- 68 H.K.D.H. Bhadeshia and D.V. Edmonds: *Met. Sci.*, **17**, (1983), p.411
- 69 O. Matsumura, Y. Sakuma, and H. Takechi: *Scripta Metall.*, **21**, (1987), p.1301
- 70 W.C. Jeong and C. H. Kim: *J. Mater. Sci.*, **20**, (1985), p.4392
- 71 G.R. Speich, V. A. Demarest, and R. L. Miller: *Metall. Trans. A*, **12A**, (1981), p.1419
- 72 C.I. Garcia and A.J. DeArdo: *Metall. Trans. A*, **12A**, (1980), p.521
- 73 D.Z. Yang, E.L. Brown, D.K. Matlock, and G. Krauss: *Metall. Trans. A*, **16A**, (1985), p.1523
- 74 T.C. Lei and J. Pan: *Institut für Werkstofftechnik TU Berlin*, (1985), p.1
- 75 E. Navara, B. Bengtsson, and K.E. Eastering: *Mater. Sci. Technol.*, **2**, (1986), p.1196

- 76 P.A. Wycliffe, G.R. Purdy, and J.D. Embury: *in Fundamentals of Dual-Phase Steels*, R.A. Kot and B.L. Bramfitt, eds., TMS-AIME, Warrendale, PA, (1981), p.59
- 77 D.J. Riehm: *M.A.Sc. Thesis*, The University of British Columbia, Vancouver, Canada, (1990)
- 78 P.G. Shewmon: *Transformations in Metals*, McCraw-Hill Book Company, New York, (1969)
- 79 L. Samuels: *Optical Microscopy of Carbon Steels*, ASM, (1980)
- 80 D.Z. Yang, E.L. Brown, D.K. Matlock, and G. Krauss: *Met. Trans. A*, **16A**, (1985), p.1385
- 81 M. Umemoto, A. Hiramatsu, A. Moriya, T. Watanabe, S. Nanba, N. Nakajima, G. Anan and Y. Higo: *ISIJ International*, **32**, (1992), p.306
- 82 E.B. Hawbolt, B. Chau, and J.K. Brimacombe: *Met. Trans. A*, **16A**, (1985), p.565
- 83 E.B. Hawbolt, B. Chau and J. K. Brimacombe: *Metall. Trans. A*, **14A**, (1983), p.1803
- 84 L.E. Collins, M. T. Shehata and J. D. Boyd: *Phase Transformations '87*, Ed. by G. W. Lorimer, (1987), p.530
- 85 W.A. Johnson and R. F. Mehl: *Trans., AIME*, **135**, (1939), p.416
- 86 M. Avrami: *J. Chem. Phys.*, **8**, (1940), p.212
- 87 M. Avrami: *J. Chem. Phys.*, **9**, (1941), p.177
- 88 A.N. Kolmogorov: *Izv. Akad. nauk USSR Ser. Matemat*, **1**, (1937), p.355
- 89 M. Avrami: *J. Chem. Phys.*, **7**, (1939), p.1103
- 90 J. W. Christian: *The Theory of Transformations in Metals and Alloys*, Part 1,

Pergamon Press, Oxford, (1975)

- 91 J.W. Cahn: *Acta Metall.*, **4**, (1956), p.449
- 92 ASTM Standard Designation: *E112-88; 1994 Book of ASTM Standards*, **3.01**, ASTM, Philadelphia, PA, (1994), p.227
- 93 E. Scheil: *Arch. Eisenhüttenw*, **12**, (1935), p.565.
- 94 J.W. Cahn: *Acta Metall.*, **4**, (1956), p.572
- 95 A. Jacot and M. Rappaz: *Acta mater.*, **47**, (1999), p.1645
- 96 M. Takahashi and H.K.D.K. Bhadeshia: *Mater. Trans., JIM*, **32**, (1991), p.689
- 97 O. Matsumura, Y. Sakuma, and H. Takechi: *Tetsu-to-Hagane*, **77**, (1991), p.1304
- 98 S. Dilney: *M.A.Sc Thesis*, The University of British Columbia, Vancouver, Canada, (1999)